Meso-Scale Simulations of Shock-Loaded Heterogeneous Explosives for Quantification of Sensitivity

H Udaykumar
IOWA UNIV IOWA CITY

03/07/2019
Final Report

REPORT DOCUMENTATION PAGE

Form Approved
OMB No. 0704-0188

The public reporting burden for this collection of information is estimated to average 1 hour per response, including the time for reviewing instructions, searching existing data sources, gathering and maintaining the data needed, and completing and reviewing the collection of information. Send comments regarding this burden estimate or any other aspect of this collection of information, including suggestions for reducing the burden, to Department of Defense, Executive Services, Directorate (0704-0188). Respondents should be aware that notwithstanding any other provision of law, no person shall be subject to any penalty for failing to comply with a collection of information if it does not display a currently valid OMB control number.
PLEASE DO NOT RETURN YOUR FORM TO THE ABOVE ORGANIZATION.

1. REPORT DATE *(DD-MM-YYYY)* 08-03-2019	2. REPORT TYPE Final Performance	3. DATES COVERED *(From - To)* 15 Aug 2015 to 14 Aug 2018

4. TITLE AND SUBTITLE	
Meso-Scale Simulations of Shock-Loaded Heterogeneous Explosives for Quantification of Sensitivity	**5a. CONTRACT NUMBER**
	5b. GRANT NUMBER FA9550-15-1-0332
	5c. PROGRAM ELEMENT NUMBER 61102F

6. AUTHOR(S) H Udaykumar, Kyung Choi	**5d. PROJECT NUMBER**
	5e. TASK NUMBER
	5f. WORK UNIT NUMBER

7. PERFORMING ORGANIZATION NAME(S) AND ADDRESS(ES) IOWA UNIV IOWA CITY 105 JESSUP HALL IOWA CITY, IA 52242 - 1316 US	8. PERFORMING ORGANIZATION REPORT NUMBER

9. SPONSORING/MONITORING AGENCY NAME(S) AND ADDRESS(ES) AF Office of Scientific Research 875 N. Randolph St. Room 3112 Arlington, VA 22203	10. SPONSOR/MONITOR'S ACRONYM(S) AFRL/AFOSR RTA1
	11. SPONSOR/MONITOR'S REPORT NUMBER(S) AFRL-AFOSR-VA-TR-2019-0047

12. DISTRIBUTION/AVAILABILITY STATEMENT
A DISTRIBUTION UNLIMITED: PB Public Release

13. SUPPLEMENTARY NOTES

14. ABSTRACT
A framework is presented for uncertainty quantification (UQ) in multi-scale models of shock-to-detonation transition (SDT) of a pressed energetic (HMX) material. The uncertainties are assumed to arise from variabilities in the material properties of HMX which are inputs to a Meso-informed Ignition and Growth (MES-IG) model. The input uncertainties are first used to quantify the variabilities in the hot-spot dynamics at the meso-scale. A Kriging-based Monte-Carlo method is used to construct probability density functions (pdfs) for the meso-scale reaction product formation rates.

15. SUBJECT TERMS
meso-scale simulation, energetic materials

16. SECURITY CLASSIFICATION OF:			17. LIMITATION OF ABSTRACT	18. NUMBER OF PAGES	19a. NAME OF RESPONSIBLE PERSON SCHMIDT, MARTIN
a. REPORT	b. ABSTRACT	c. THIS PAGE			
Unclassified	Unclassified	Unclassified	UU		19b. TELEPHONE NUMBER *(Include area code)* 703-588-8436

Standard Form 298 (Rev. 8/98)
Prescribed by ANSI Std. Z39.18

Final Report: Meso-Scale Simulations of Shock-Loaded Heterogeneous Explosives for Quantification of Uncertainty

PI: H.S. Udaykumar

Professor, Department of Mechanical and Industrial Engineering

The University of Iowa, Iowa City, IA-52242

1. INTRODUCTION

Safety and performance control of energetic materials, such as propellants, explosives and pyrotechnics, demands characterization of the sensitivity of such materials to transient loads. The sensitivity of a heterogeneous energetic material (HE) to shock or impact loading is an intrinsically multi-scale phenomenon. The reactive heat release and transition to detonation observed at the system (macro-) scale is initiated at the meso-scale, i.e. at the level of heterogeneities such as interfaces and defects (voids, cracks) in the material. Prediction of the response of a HE therefore must account for the sub-scale (typically meso-scale) thermo-mechanics that initiates the shock-to-detonation transition. Modeling of such a multi-scale process hinges critically on the fidelity of the material models used in the computations of the meso-scale response, in particular the dynamics of void collapse and hotspot formation. In a multi-scale simulation of the response of a HE, the macro-scale model typically homogenizes the meso-scale physics; crucial energy release terms from the meso-scale then serve as closure models, appearing as source terms in the macro-scale governing equations. These closure models have typically been supplied through semi-empirical phenomenological models such as ignition-and-growth , CREST , SURF and others . Such so-called "burn models" have to be fit to data from expensive and time-consuming physical experiments . An alternative route, made possible by advances in computational hardware and software resources, is to construct burn models by using numerical (*in silico*) experiments .

To be useful in predictive modeling of the response of HEs, numerical simulations of the meso-scale dynamics must accurately portray the thermo-mechanical events at the meso-scale. One important physical mechanism for meso-scale energy localization is void or pore collapse in the heterogeneous energetic material. It has been shown experimentally and computationally that shock-induced void collapse in the energetic material can lead to intense hot spots that can potentially initiate thermal runaway and SDT. Simulations of void collapse have been performed by various researchers to predict the characteristics of hotspots formed due to collapse of voids of different shapes and sizes. Experiments, meso-scale continuum simulations, and nano-scale MD simulations all point to the very high temperatures reached upon void collapse. However, at least in meso-scale continuum mechanical calculations, there is sparse understanding regarding the effect of uncertainties in material properties and models used in the meso-scale model on the predicted hotspot characteristics, chiefly the temperature of the hotspot. This work provides the first quantification of the effect of parametric uncertainties on the predicted hotspot characteristics for HMX, a commonly used HE material.

Uncertainty in the material models propagates from the meso-scale to the macro-scale because the macro-scale response of the energetic material is intimately linked to meso-scale physics. In recent work , a multi-scale model was developed for the simulation of shock response of neat pressed HMX. A hierarchical

approach was used, where the energy deposition rate in a macro-scale control volume was supplied in the form of an ignition-and-growth surrogate model. The hot spot ignition and growth rates were obtained from the meso-scale calculations and cast as surrogate models to represent the functions $\dot{F}_{ignition}(P_s, D_{void})$ and $\dot{F}_{growth}(P_s, D_{void})$ respectively, where P_s is the shock pressure and D_{void} is the void size. The surrogate model was developed from an ensemble of meso-scale simulations of reactive void collapse. Each simulation of reactive void collapse was performed using an Eulerian sharp-interface approach , using an elasto-plastic material description for HMX and Tarver's 3-equation chemical kinetics model for heat release to calculate the temperature field resulting from the collapse of the void. The functions $\dot{F}_{ignition}(P_s, D_{void})$ and $\dot{F}_{growth}(P_s, D_{void})$ were then used to close the macro-scale equations and predict the run-to-detonation and James curves for a pressed HMX of given microstructure (porosity and void sizes). However, two questions arise in such a multi-scale approach:

- How do uncertainties in the model parameters (thermo-physical property values, reaction rates) impact on the predicted hot spot characteristics (temperature and size of the hot spot) and the calculated meso-scale rates $\dot{F}_{ignition}$ and $\dot{F}_{growth}$?
- How do the resulting uncertainties in the surrogate models, i.e. the closure functions $\dot{F}_{ignition}(P_s, D_{void})$ and $\dot{F}_{growth}(P_s, D_{void})$, propagate to and impact the predicted macro-scale quantities of interest (QoIs), namely the run-to-detonation distances and the James critical energy for initiation?

To date, there has been little work in the literature to provide insights into these issues. Characterizing parametric uncertainty and propagation of uncertainty across scales is necessary to build confidence in multi-scale models. In addition, if the sensitivity of the predicted QoIs to the uncertainties in parameters can be established, efforts can be directed (by experimentalists, material and chemistry modelers and MD practitioners) to focus on the most significant parameters first. Thus, uncertainty quantification and sensitivity analysis will provide important information to the energetic materials research community.

1.1. Parametric uncertainty quantification and sensitivity analysis

Uncertainty quantification (UQ) in materials modeling has been a research topic for some time. A variety of approaches for parametric uncertainty quantification (UQ) have been developed for last couple of decades e.g. asymptotic parameterization [1], polynomial chaos [4], alternative sampling methods [5], and Bayesian approaches [6]. Significant efforts have been made to investigate the uncertainty propagation across different scales, e.g. from molecular-scale to microstructures [3] especially in research on material science aspects [2]. However, in the context of energetic materials, there has been limited study on quantifying the uncertainties in material properties, micro-structures and reaction kinetics on the sensitivity of the material.

For the simulation of heterogeneous energetic materials with an underlying microstructure, where the initiation of reactions needs to be captured, the multi-scale approach must contend with significant uncertainties in material parameters. For complex materials such as HEs responding to high pressure and temperature scenarios, the material models can be challenging to pin down [Sewell and Menikoff]. For the available material models, the model parameters are difficult to establish; extreme loading conditions and difficulty in handling energetic materials present roadblocks to establishing thermo-physical properties.

Therefore, available experimental parameters for properties such as specific heats, melting points, yield stresses, bulk moduli etc. can vary over a large range, depending on whether these parameters are obtained from physical experiments or first-principles (typically MD) calculations . Later in this work we tabulate the available data for such parameters for the case of HMX--a relatively well-studied material-- displaying the rather large uncertainties in the open literature. The considerable uncertainties in properties and models can translate into uncertainties in computed hotspot intensities and energy localization at the meso-scale. Furthermore, uncertainties in the closure models constructed from meso-scale calculations can then propagate to macro-scale QoI calculations. In the specific context of pressed HMX, the uncertainties can be classified into four types: 1) variabilities in loads, 2) uncertainty in thermo-mechanical properties, 3) uncertainty in reactive kinetics and chemical properties and 4) variabilities due to the stochasticity of the microstructure itself. It is noteworthy that all these fall in the class of irreducible or aleatory uncertainties. In contrast to epistemic uncertainties, which are reducible and can be reduced by improving material models or numerical accuracy, the variabilities in the above categories are not easily mitigated. This report will focus solely on the uncertainty in thermo-mechanical properties. Assessing the uncertainties due to stochasticity in the meso-structure, for example, is a subject of ongoing work that will be reported on separately.

The present work determines the uncertainties in the macro-scale quantity of interest (QoI) due to variabilities in the material properties of HMX. A commonly used QoI, which defines the sensitivity of the energetic material to applied loads and appears in the so-called Pop-plot , is the run-to-detonation distance (RTD) *h* of the material. The RTD is experimentally determined for a sample of HE by performing an impact experiment, for example a low-speed "gap" test or high-speed flyer impact test . The distance into the sample at which the resulting stress/shock wave transitions to a detonation front is measured and plotted against the impact pressure to obtain the Pop-plot . Of particular interest in this work is the high-speed impact regime, characterized by flyer-plate experiments, i.e. the scenario of shock-to-detonation transition (SDT). The run-to-detonation distances are computed using a recently developed multiscale model, the Meso-scale Informed Ignition and Growth (MES-IG) model, for simulating SDTs in high-speed regime. The variabilities in the material properties of HMX are propagated from the meso-scale to the continuum/macro-scale in the MES-IG model, and the uncertainties in the run-to-detonation distances are quantified.

The rest of the report is organized as follows. Section 2 briefly describes the MES-IG model and explains the procedures for quantifying the uncertainties at the meso- and the macro-scales. The propagation of the uncertainty from the meso- to the macro-scale and the uncertainties in the Pop-plots are shown in Section 3. The key conclusions and directions for future work are discussed in Section 4.

2. METHODS FOR UNCERTAINTY QUANTIFICATION IN MULTISCALE MODELS FOR SDT IN HMX

2.1 The multiscale MES-IG model for SDT in HE materials

MES-IG is a multi-scale framework for simulating SDT in energetic materials and has the following three components:

Component 1: A homogenized macro-scale model of the porous reactive material: At the macro-scale, the meso-structural heterogeneities in the material (voids, grain boundaries, defects etc.) are treated as subgrid-

scale/unresolved features. The macro-scale representation of the material is a coarse-grained/ homogenized mixture of reactants and products. Computations of the run-to-detonation h are performed for such a homogenous model, as shown in Figure 1.

Component 2: A meso-scale computational model for reactive void-collapse simulations: At the meso-scale, the energy localization at hotspots is fully resolved by accounting for the voids and defects in the material. Calculations are performed to follow the reactive void-collapse and the resulting hotspot evolution. Ensembles of such computations are used to extract information on the ignition and growth rates of hotspots.

Component 3: A surrogate model to bridge the meso- and the macro- scales : The energy localization due to hotspot formation at the subgrid (meso-) scale is transmitted to the macro-scale through surrogate models that link the meso-scale hotspot dynamics to the macro-scale response.

The above three components are summarized next.

2.1.1. Component 1: The macro-scale model for prediction of SDT

At the macro-scale, all voids, defects and grain-boundaries in the microstructure of the material are treated as sub-grid/unresolved scale features. The macro-scale representation of the material is a homogenized mixture of solid HMX and gaseous reactant products, described by the system of equations of the form:

$$\mathbf{D}(\mathbf{a}|\lambda) = 0 \tag{1}$$

In the above equation, the operator $\mathbf{D}$ denotes the set of hyperbolic conservation laws and constitutive relations for the material, and the vector $\mathbf{a}$ denotes the thermo-mechanical flow variables such as the density, velocity components and internal energy of the macro-scale mixture. The transition of an imposed shock to a detonation wave at the macro-scale is marked by the transformation of the mixture from a cold unreacted solid Hugonoit to a reaction product mixture Hugonoit, following the mixture Rayleigh line. The state of the mixture on the Rayleigh line is defined by the reaction-progress variable λ, which is the mass fraction of the reaction products in a macro-scale control volume. When $\lambda = 0$, the material is an unreacted explosive; when $\lambda = 1$, the reaction is complete and the macro-scale material is in the CJ state. To close the macro-scale system of equations, an evolution equation for λ is necessary. In the MES-IG model, the evolution equation for λ follows the Ignition and Growth model :

$$\frac{d\lambda}{dt} = \dot{\lambda}_{ignition}H\big(\lambda_{ignition,max} - \lambda\big) + \dot{\lambda}_{growth}H\big(\lambda - \lambda_{ignition,max}\big) \tag{2}$$

where *H* is the Heaviside function :

$$H(\Delta\lambda) = \begin{array}{l} 0, \text{for } \Delta\lambda < 0 \\ 1, \text{for } \Delta\lambda \geq 0 \end{array} \tag{3}$$

Thus, Eqn. (2) relies on an initial ignition phase (the first term on the RHS of Eq. (2)), a later growth phase (the second term on RHS of Eq. (2)), and a switching constant, $\lambda_{ignition,max}$ (selected to be 0.02 in this report) that marks the transition from the ignition to the growth phase. In the MES-IG model, instead of phenomenological closure laws, $\dot{\lambda}_{ignition}$ and $\dot{\lambda}_{growth}$ are machine-learned from high-fidelity meso-scale

computations of reactive void collapse. As shown in Sen et al. , $\dot{\lambda}_{ignition}$ and $\dot{\lambda}_{growth}$ are connected to the corresponding meso-scale product formation rates, $\dot{F}_{ignition}$ and $\dot{F}_{growth}$ via the following equation

$$\dot{\lambda}_{ignition} = \phi\dot{F}_{ignition}; \; \dot{\lambda}_{growth} = \phi\dot{F}_{growth} \qquad (4)$$

where ϕ is the porosity of the material. The quantities $\dot{F}_{ignition}$ and $\dot{F}_{growth}$ track the mass fraction of reaction products accumulated at different stages of void-collapse in the meso-scale computations. The meso-scale computational model and the procedure for obtaining $\dot{F}_{ignition}$ and $\dot{F}_{growth}$ are described in details in Sen et al. and are summarized briefly in the next section.

2.1.2. Component 2: The meso-scale model for reactive void-collapse

At the meso-scale, the energy localization at hot-spots is fully resolved by accounting for the voids and defects in the energetic material. Calculations are performed to follow the reactive void collapse and the resulting hot-spot evolution. The meso-scale computational model is represented by the following system:

$$\mathbf{f}\left(\mathbf{b}\big|\boldsymbol{\pi}^{(N)}\right) = \mathbf{0} \qquad (5)$$

where the operator $\mathbf{f}$ describes the conservation laws, constitutive equations and the chemical kinetic equations of the meso-scale computational model, and $\mathbf{b}$ denotes the meso-scale flow variables such as density, velocity components, deviatoric stresses, pressure, internal energy etc. $\boldsymbol{\pi}^{(N)}$ is an N-dimensional vector, consisting of the material properties of solid HMX at the meso-scale, such as the reference density, yield strength, specific heat, bulk modulus etc. Chemical decomposition of HMX is modeled by the Tarver 3-equation model [16] via four different species, Y_1 through Y_4, as explained in Sen et al. . The meso-scale computations track the mass of the final reaction product Y_4 at different stages of void-collapse. The meso-scale product formation rates, $\dot{F}_{ignition}$ and $\dot{F}_{growth}$, are computed from simulations of void collapse, hotspot formation and subsequent growth. $\dot{F}_{ignition}$ is obtained from the mass of the species Y_4 during the initial stages of void-collapse, while $\dot{F}_{growth}$ is obtained from the mass of Y_4 during the later stages, i.e. after the void fully collapses and the hot-spot grows, as explained in the works of Sen et al and Nassar et al. .

2.1.3. Component 3: Surrogate models to bridge scales

The quantities $\dot{F}_{ignition}$ and $\dot{F}_{growth}$, obtained from the meso-scale computations, are used to compute the macro-scale reaction progress variables $\dot{\lambda}_{ignition}$ and $\dot{\lambda}_{growth}$ using the following procedure:

1. First, ensembles of meso-scale computations of reactive void-collapse are performed to compute $\dot{F}_{ignition}$ and $\dot{F}_{growth}$ for different input pressures, P_s, and different void diameters, D_{void}.
2. The computed $\dot{F}_{ignition}$ and $\dot{F}_{growth}$ are used as inputs for training surrogate models of the form $\dot{F}_{ignition}(P_s, D_{void})$ and $\dot{F}_{growth}(P_s, D_{void})$.
3. The macro-scale reaction progress variables, $\dot{\lambda}_{ignition}$ and $\dot{\lambda}_{growth}$, are obtained from the surrogates $\dot{F}_{ignition}(P_s, D_{void})$ and $\dot{F}_{growth}(P_s, D_{void})$ using Eqn. (4). *In silico* flyer plate impact tests are performed on the macro-scale system. The macro-scale computations probe the surrogates for $\dot{\lambda}_{ignition}$ and $\dot{\lambda}_{growth}$ on the fly for calculating the product mass fraction based on the local pressure $p = P_s$ and the void-diameter D_{void} in the macroscale control volume. Once $\dot{\lambda}_{ignition}$ and $\dot{\lambda}_{growth}$

are obtained, Eqns. (1)-(2) are solved for computing run-to-detonation distances, h, which are taken to be distances at which the incident shock wave reaches the Von-Neumann pressure in the material.

In this report, the computed run-to-detonation distances and the uncertainties therein are compared against the pop-plots of the experiments reported by Massoni et al [17]. The void sizes are assumed to lie in the range identified by Massoni et al.[17] and the surrogates are constructed for $D_{void} = 0.5$ µm; i.e. the uncertainties due to void-size distributions are neglected and $\dot{F}_{ignition}$ and $\dot{F}_{growth}$ are assumed to be functions of pressure alone. Furthermore, the pressed HMX in the experiments [18] has a TMD of 96%. Because of such low porosity, only isolated voids are considered at the meso-scale for computing $\dot{F}_{ignition}$ and $\dot{F}_{growth}$. The porosity of the material is fixed at $\phi = 3\%$ and surrogates for $\dot{F}_{ignition}$ and $\dot{F}_{growth}$ are constructed by assuming single cylindrical voids of diameter $D_{void} = 0.5$ µm at the meso-scale. Methods for constructing more general surrogates such as those for non-cylindrical voids as well as for a field of voids are discussed in details in previous works.

2.2. Methods for quantifying the uncertainties in h

To quantify the uncertainties in h, first the uncertainties in $\dot{F}_{ignition}$ and $\dot{F}_{growth}$ due to variabilities in $\boldsymbol{\pi}^{(N)}$ are studied. These are then propagated to the macro-scale to quantify the uncertainties in h due to variabilities in $\boldsymbol{\pi}^{(N)}$.

The vector $\boldsymbol{\pi}^{(N)}$ comprises several material properties of solid HMX, such as reference density, yield strength, specific heat, Gruneisen parameter, melting temperature, among others. Performing an uncertainty quantification on such a high dimensional input parameter space is computationally formidable. Therefore, in this work, variabilities in $\boldsymbol{\pi}^{(N)}$ are assumed to arise due to variabilities in only six material properties. The material properties used in the present work are the following.

1. Specific heat, C_p: Variabilities in C_p affect the meso-scale computational model in two ways. First, C_p is used to compute the isochoric specific heat C_v (Eq. (A9)), which is used in the equation of state (A5) of the material. Therefore, variability in C_p affects the volumetric work term in the conservation law for the internal energy of the material (Eqn. A3). Second, C_p is used in Eq. ((A10) to compute the increase in enthalpy due to the heat released from the chemical reactions at the meso-scale. Because this formation enthalpy is used to compute the source term, $\dot{\mathcal{E}}$, in the energy equation (Eqn. A3), variabilities in C_p affect the energy deposited in the material due to chemical reactions at hot-spots.

   In the past, experimental techniques as well as molecular dynamic simulations have been performed to obtain the values of C_p for HMX [16, 20-23], as summarized in Figure 2(a). Most of the specific heat data in the references are dependent on temperatures while the Molecular Dynamics (MD) data by Long et al. [21] is a constant. In the MES-IG model, hot-spots in the material are defined as regions where the local temperature is above 900 K; it is noted in the figure that above 900K, the variation of C_p with temperature is modest. Therefore, as a simplified approximation, C_P is assumed to be independent of the temperature.

2. Bulk Modulus, K_T : The bulk modulus is used in Eqn. (A9) to compute C_v from C_p; therefore, an uncertainty in K_T results in variability in C_v. Because C_v appears in the caloric equation of state (Eq. (A8)) in the meso-scale computational model, variabilities in K_T result in uncertainties in the volumetric deformation of solid HMX under shock loading. Furthermore, as described in the appendix, C_v is used

to compute the increase in internal energy of the material due to chemical reactions in HMX. Thus, variabilities in K_T also result in uncertainties in the source term, $\dot{\mathcal{E}}$, in the energy equation at the meso-scale (Eq. (A3)). In this work, values of K_T for HMX are obtained from experimental and MD estimates, as reported in the literature [21, 24-31] and are summarized in Figure 2(b).

3. <u>Yeild Strength, σ_Y</u> : Variabilities in the yield strength of HMX affect the plastic deformation and the deviatoric work terms in the conservation laws for momentum and energy at the meso-scale (Eqns. A2- A3) respectively. Unlike K_T and C_p, variability in σ_Y only affects the inert collapse profiles of the voids at the meso-scale and does not play a role in the meso-scale chemical reaction dynamics. In the present work, values for σ_Y are obtained from fits to experimental data [20], VISAR measurements [35], drop-weight experiments [36], MD simulations [37], and from those used in the computational work by Gilbert et al [38]. A summary of the yield strength values is shown in Figure 2c.

4. <u>Coefficient of thermal expansion, α:</u> Similar to K_T, the thermal expansion coefficient α is used in Eqn. (A9) to compute C_v from C_p. Therefore, variabilities in α result in uncertainties in the volumetric deformation of HMX, as well as in the source term, $\dot{\mathcal{E}}$, in the energy equation (Eq. (A3)). The values of α used in the current work are summarized in Figure 2d and are obtained from measurements of α using X-ray diffraction techniques [43, 44] and MD simulations [21].

5. <u>Gruneisen Paratemeter, Γ</u>: The Grüneisen parameter appears in the meso-scale equation of state (A5) of HMX and is typically obtained by empirical fits to the isotherm of the material [32]. In this work, the Γ is assumed to vary between 0.7 [33] and 1.1 [20].

6. <u>Thermal Conductivity, k</u>: Similar to C_p, the thermal conductivity k is used to compute the increase in enthalpy in the material due to the heat released from chemical reactions at the meso-scale (Eqn. A11). Therefore, uncertainties in k affect the source term $\dot{\mathcal{E}}$, in the energy equation (Eqn. A3). In this work, values of k are obtained from experimental data [16, 23, 39, 40] as well as from MD simulations [41, 42], as summarized in Figure 2e.

In summary, six material properties defining the set $\boldsymbol{\pi}^{(6)} = [C_p, K_T, \sigma_Y, \alpha, \Gamma, k,]$ are selected to quantify the uncertainties in the QoI (h) obtained from the MES-IG model. Table 1 summarizes the maximum and minimum values of $\boldsymbol{\pi}^{(6)}$ used for uncertainty quantification in this work. Before performing a global uncertainty quantification in the six-dimensional parameter space, a preliminary sensitivity analysis of $\dot{F}_{ignition}$, and $\dot{F}_{growth}$ with respect to the variabilities in the individual components of $\boldsymbol{\pi}^{(6)}$ is conducted. The sensitivity analysis is performed using a variable pre-screening algorithm, as discussed next.

2.2.1. Procedure for preliminary variable screening

The objective of the variable screening is to rank the six variables in $\boldsymbol{\pi}^{(6)}$ according to the sensitivity of $\dot{F}_{ignition}$, and $\dot{F}_{growth}$ to those variables. The screening is performed using the Morris variable screening procedure . The screening process calculates the sensitivity of $\dot{F}_{ignition}$, and $\dot{F}_{growth}$ to variations in $C_p, K_T, \sigma_Y, \alpha, \Gamma$, and k at random locations in the parameter space. The key concept underlying this procedure is the elementary effect, which is a measure of the change in $\dot{F}_{ignition}$, and $\dot{F}_{growth}$ when a single variable is perturbed. For a function $y = f(x_i)$ with k independent variables $x_i, i = 1,2, \dots k,$, an elementary effect d_i on y due to a perturbation in the basis x_i is defined by

$$d_i(\boldsymbol{x}) = \frac{y(x_1, x_2, \cdots, x_{i-1}, x_i + \Delta, x_{i+1}, \cdots, x_k) - y(\boldsymbol{x})}{\Delta} \qquad (6)$$

where $x_1, x_2, \cdots, x_k$ is a baseline set of independent variables, and Δ is the change in the variable x_i. Following the guideline in previous work [19], Δ is set to $\frac{1}{4}(x_{i,max} - x_{i,min})$ in this report, where $x_{i,max}$ and $x_{i,min}$ are the upper and the lower limits of the variable x_i in the parameter space. The limits for the variables in $\boldsymbol{\pi}^{(6)}$ are summarized in Table 1.

The elementary effect for k independent variables is calculated by performing $k + 1$ computations. To do this, a $(k + 1) \times k$ matrix $\mathbf{B}$ is created, where each row of $\mathbf{B}$ provides a set of input variables for a single simulation. The first row is a randomly generated set of input variables x_i; each subsequent row varies one input at a time by Δ. Running all the $k + 1$ simulations produces a randomized elementary effect for each of the n input variables. If r elementary effects are desired for each input variable, the entire set of prescreening test cases $\mathbf{X}$ is defined by producing multiple versions of $\mathbf{B}$:

$$\mathbf{X} = [\mathbf{B}_1 \quad \mathbf{B}_2 \quad \cdots \quad \mathbf{B}_r]^T \qquad (7)$$

where the individual matrices $\mathbf{B}_i$ are initialized at different locations in the parameter space. In the present work, $\boldsymbol{\pi}^{(6)}$ comprises 6 independent variables (*i.e.* k=6), and the screening process is initiated at 4 random locations in the $\boldsymbol{\pi}^{(6)}$ parameter space (i.e. r=4), thereby leading to $(6 + 1) \times 4 = 28$ simulations. The mean and standard deviations of the elementary effects at the 4 random locations are computed. A large absolute value of the mean or a high standard deviation of the elementary effects of a variable x_i implies that y is sensitive to variabilities in x_i. Thus, y is more sensitive to x_i than x_j, $i, j = 1,2, ..., k; i \neq j$, if the mean of the elementary effect of x_i is greater than that of x_j. If the means of the elementary effects of x_i and x_j are comparable, then y is more sensitive to x_i than x_j if the standard deviation of the elementary effects of x_i is greater than that of x_j.

It is noted that unlike sensitivity measurement methods such as Variance Partitioning using Sobol indices or feature selection methods such as LASSO regularization , the Morris method does not sweep the input space $\boldsymbol{x}$ globally for variable screening. Instead, the method determines the sensitivity of y only at discreet windows defined by the matrices $\mathbf{B}_i$, $i = 1,2, ..., r$, in the parameter space. However, the method is computationally inexpensive compared to the aforementioned global sensitivity measurement techniques or feature selection methods, and has been reported to reliably rank the variables x_i in order of their sensitivity of y for a wide variety of applications . Therefore, in this work, the Morris method is chosen to perform a preliminary variable screening to rank the parameters of $\boldsymbol{\pi}^{(6)}$, according to their sensitivity on $\dot{F}_{ignition}$, and $\dot{F}_{growth}$.

Figure 3 shows the elementary effects of the six independent variables, $\boldsymbol{\pi}^{(6)} = [C_p, K_T, \sigma_Y, \alpha, \Gamma, k]$ on $\dot{F}_{ignition}$, and $\dot{F}_{growth}$ at $P_s = 22$ GPa. As shown in the figure, the mean and the standard deviations of the elementary effects of C_p are the highest for both $\dot{F}_{ignition}$, and $\dot{F}_{growth}$, i.e. $\dot{F}_{ignition}$, and $\dot{F}_{growth}$ are most sensitive to variabilities in C_p. Furthermore, in Figure 3b, it is observed that for $\dot{F}_{ignition}$, the means

of the elementary effects of K_T and α are higher compared to those for Γ, σ_Y and k. On the other hand, for $\dot{F}_{growth}$, the means of the elementary effects of σ_Y and α are higher than those of γ, K_T and k. Because the elementary effects of the Gruneisen coefficient Γ and the thermal conductivity k are relatively small (Figure 3), $\dot{F}_{ignition}$, and $\dot{F}_{growth}$ are least sensitive to Γ and k compared to the other components of $\boldsymbol{\pi}^{(6)}$. The relative insensitivity with respect to the Gruniesen parameter has been remarked on by Menikoff ; the insensitivity to thermal conductivity k is perhaps due to the fact that in the void collapse-generated hotspot phenomena, the diffusion time-scale is larger than the inertial and reaction time scales, i.e. inertia and chemical reaction heat release are the dominant physical processes. Therefore, in the remaining parts of the report, the inferences from the Morris screening algorithm will be used to discard the variables, Γ and k, for the UQ and the uncertainties of $\dot{F}_{ignition}$, and $\dot{F}_{growth}$ will be quantified only for the four-dimensional parameter space given by $\boldsymbol{\pi}^{(4)} = [C_p, K_T, \sigma_Y, \alpha]$.

2.2.2. Surrogate-based Monte-Carlo method for quantification of uncertainty in $\dot{F}_{ignition}$, and $\dot{F}_{growth}$

To quantify the uncertainties in $\dot{F}_{ignition}$, and $\dot{F}_{growth}$, the material parameters, $\boldsymbol{\pi}^{(4)} = [C_p, K_T, \sigma_Y, \alpha]$ are treated as random variables, $\widetilde{\boldsymbol{\pi}}^{(4)} = [\tilde{C}_P \quad \widetilde{K}_T \quad \tilde{\sigma}_Y \quad \tilde{\alpha}]$ where the tilde is used to distinguish random variables from their deterministic counterparts. It is assumed that $\widetilde{\boldsymbol{\pi}}^{(4)}$ follows a normal distribution with mean $\boldsymbol{\mu}_{\boldsymbol{\pi}}$ and variance $\boldsymbol{\sigma}_{\boldsymbol{\pi}}^2$, i.e.

$$\widetilde{\boldsymbol{\pi}}^{(4)} \sim N(\boldsymbol{\mu}_{\boldsymbol{\pi}}, \boldsymbol{\sigma}_{\boldsymbol{\pi}}^2) \tag{8}$$

where $\boldsymbol{\mu}_{\boldsymbol{\pi}} = [\mu_{C_p} \quad \mu_{K_T} \quad \mu_{\sigma_Y} \quad \mu_{\alpha}]$ and $\boldsymbol{\sigma}_{\boldsymbol{\pi}} = [\sigma_{C_P} \quad \sigma_{K_T} \quad \sigma_{\sigma_Y} \quad \sigma_{\alpha}]$ are respectively the vectors of the mean values and the standard deviations of $\boldsymbol{\pi}^{(4)}$. Because the parameters C_p, K_T, σ_Y, and α, are independent thermomechanical properties of the HE material, these are treated as uncorrelated random variables, with zero covariances. The means $[\mu_{C_p} \quad \mu_{K_T} \quad \mu_Y \quad \mu_{\alpha}]$, and the standard deviations $[\sigma_{C_P} \quad \sigma_{K_T} \quad \sigma_Y \quad \sigma_{\alpha}]$ are estimated as the averages and the standard deviations of the values of the material parameters obtained from literature (Figures 3-7). For example, μ_{C_P} and σ_{C_P} are the average and the standard deviation of the C_p values shown in Figure 3. Once $\boldsymbol{\mu}_{\boldsymbol{\pi}}$ and $\boldsymbol{\sigma}_{\boldsymbol{\pi}}^2$ are determined, probability density functions (pdfs) for $\dot{F}_{ignition}$, and $\dot{F}_{growth}$ are constructed using a surrogate-based Monte-Carlo method. The procedure for constructing the pdfs is as follows:

1. First, the pdfs, $\widetilde{\boldsymbol{\pi}}^{(4)}$, are sampled at $k = 10^6$ random points to generate the Monte Carlo (MC) points for uncertainty quantification. The MC points are chosen to lie in the range, $\boldsymbol{\mu}_{\boldsymbol{\pi}} - 3\boldsymbol{\sigma}_{\boldsymbol{\pi}} < \widetilde{\boldsymbol{\pi}}^{(4)} < \boldsymbol{\mu}_{\boldsymbol{\pi}} + 3\boldsymbol{\sigma}_{\boldsymbol{\pi}}$, and are sampled using the code RAMDO .
2. Next, ensembles of meso-scale void-collapse simulations are performed for m_1 different values of $\widetilde{\boldsymbol{\pi}}^{(4)}$ lying in the range $\boldsymbol{\mu}_{\boldsymbol{\pi}} - 3\boldsymbol{\sigma}_{\boldsymbol{\pi}} < \widetilde{\boldsymbol{\pi}}^{(4)} < \boldsymbol{\mu}_{\boldsymbol{\pi}} + 3\boldsymbol{\sigma}_{\boldsymbol{\pi}}$. These locations for the initial computations are chosen randomly by a Latin hypercube sampling technique. The simulations are performed at $P_s = \hat{P} = 22\ GPa$ to compute the values of $\dot{F}_{ignition}$, and $\dot{F}_{growth}$ at these m_1 locations in the parameter space.
3. The $\dot{F}_{ignition}$, and $\dot{F}_{growth}$ computed from Step 1 are used as inputs to a Dynamic Kriging algorithm (DKG) to construct initial surrogates for $\dot{F}_{ignition}$, and $\dot{F}_{growth}$ as functions of $\widetilde{\boldsymbol{\pi}}^{(4)}$. The DKG method also identifies m_2 new locations in the parameter space $\boldsymbol{\mu}_{\boldsymbol{\pi}} - 3\boldsymbol{\sigma}_{\boldsymbol{\pi}} < \widetilde{\boldsymbol{\pi}}^{(4)} < \boldsymbol{\mu}_{\boldsymbol{\pi}} + 3\boldsymbol{\sigma}_{\boldsymbol{\pi}}$ for performing further meso-scale simulations. These new locations are based on an in-built adaptive sampling technique of the DKG algorithm, described in detail in Zhao et al. .

4. Additional meso-scale computations are performed at the m_2 locations identified by the DKG method in step 2. The process for step 2 is repeated to construct improved surrogates for $\dot{F}_{ignition}$, and $\dot{F}_{growth}$ using the $m_1 + m_2$ simulation results. Similar to step 2, the DKG method further identifies m_3 new locations in the parameter space for additional meso-scale computation.

5. The procedure is repeated to compute $\dot{F}_{ignition}$, and $\dot{F}_{growth}$ at $m_1 + m_2 + \cdots + m_n$ points in the parameter space until the mean square error of the predicted variance of the DKG method falls below 1% , where the surrogates of $\dot{F}_{ignition}$ and $\dot{F}_{ignition}$ are assumed to have converged. In the present work, the surrogates converged for $m_1 + m_2 + \cdots + m_5 = 125$ meso-scale (reactive void collapse) computations.

6. The converged surrogates obtained in the previous step are then probed at the $k = 10^6$ MC points obtained in Step 1 to construct the pdfs of $\dot{F}_{ignition}$, and $\dot{F}_{growth}$. The pdfs, hereafter denoted by $\tilde{\dot{F}}_{ignition}(\hat{P})$ and $\tilde{\dot{F}}_{growth}(\hat{P})$, are joint probability distributions due to simultaneous variabilities in all the four material parameters of $\tilde{\boldsymbol{\pi}}^{(4)}$ at $P_s = \hat{P} = 22\ GPa$. In addition to the joint distributions, conditional pdfs for $\dot{F}_{ignition}$, and $\dot{F}_{growth}$ are also computed to study the effect of variabilities of the individual components of $\tilde{\boldsymbol{\pi}}^{(4)}$. For example, the conditional pdf $\tilde{\dot{F}}_{ignition}(\tilde{C}_P | \mu_\alpha, \mu_{\sigma_Y}, \mu_{K_T})$ is computed by probing the surrogate for $\dot{F}_{ignition}$ of step 4 at $k = 10^6$ points lying in the range $[\mu_{C_P} - 3\sigma_{C_P} \quad \mu_{K_T} \quad \mu_{\sigma_Y} \quad \mu_\alpha] < \tilde{\boldsymbol{\pi}}^{(4)} < [\mu_{C_P} + 3\sigma_{C_P} \quad \mu_{K_T} \quad \mu_{\sigma_Y} \quad \mu_\alpha]$. This conditional pdf shows the variabilities in $\dot{F}_{ignition}$ due to variations in C_p alone, while K_T, α and σ_Y are held constant. Similar conditional pdfs are also constructed for $\tilde{\dot{F}}_{ignition}(\tilde{\alpha} | \mu_{C_P}, \mu_{\sigma_Y}, \mu_{K_T})$, $\tilde{\dot{F}}_{ignition}(\tilde{\sigma}_Y | \mu_{C_P}, \mu_\alpha, \mu_{K_T})$, $\tilde{\dot{F}}_{ignition}(\tilde{K}_T | \mu_{C_P}, \mu_\alpha, \mu_{\sigma_Y})$ as well as for $\tilde{\dot{F}}_{growth}(\tilde{C}_P | \mu_\alpha, \mu_{\sigma_Y}, \mu_{K_T}), \tilde{\dot{F}}_{growth}(\tilde{\alpha} | \mu_{C_P}, \mu_{\sigma_Y}, \mu_{K_T}), \tilde{\dot{F}}_{growth}(\tilde{\sigma}_Y | \mu_{C_P}, \mu_\alpha, \mu_{K_T})$ and $\tilde{\dot{F}}_{growth}(\tilde{K}_T | \mu_{C_P}, \mu_\alpha, \mu_{\sigma_Y})$.

The above procedure is used to quantify the uncertainties in the meso-scale quantities of interest, viz $\dot{F}_{ignition}$, and $\dot{F}_{growth}$ due to variabilities in $\boldsymbol{\pi}^{(4)}$. These uncertainties are propagated to the macro-scale reaction progress variables, $\dot{\lambda}_{ignition}$ and $\dot{\lambda}_{growth}$, using the following procedure.

2.2.3. Procedure for estimating the uncertainties in $\dot{\lambda}_{ignition}$ and $\dot{\lambda}_{growth}$

The pdfs, $\tilde{\dot{F}}_{ignition}(\hat{P})$ and $\tilde{\dot{F}}_{growth}(\hat{P})$, are constructed only for $P_s = \hat{P}$; but macro-scale computations require pdfs for $\dot{F}_{ignition}$ and $\dot{F}_{growth}$ at different values of P_s to compute uncertainties in run-to-detonation distances. However, obtaining pdfs for $\dot{F}_{ignition}$, and $\dot{F}_{growth}$ over a wide range of P_s is computationally expensive, since it requires mesoscale simulations not only at different values of $\boldsymbol{\pi}^{(4)}$ (Section 2.2.3), but also at different values of P_s. To reduce the computational burden, this work assumes that the uncertainties in $\dot{F}_{ignition}$ and $\dot{F}_{growth}$ are independent of P_s. In other words, while the mean value of the surrogates for $\dot{F}_{ignition}$ and $\dot{F}_{growth}$ depend on P_s, the variability in the surrogates due to uncertainties in material parameters are assumed to remain the same at all values of P_s. Under this assumption, the pdfs $\tilde{\dot{F}}_{ignition}(\hat{P})$ and $\tilde{\dot{F}}_{growth}(\hat{P})$, can be used to propagate the uncertainties in $\dot{F}_{ignition}$ and $\dot{F}_{growth}$ at different P_s values, i.e. for $P_s \neq 22\ GPa$, using the steps described below.

1. First, deterministic surrogates for $\dot{F}_{ignition}$ and $\dot{F}_{growth}$ are constructed as functions of P_s for fixed $\boldsymbol{\pi}^{(4)}$ i.e. by fixing $\boldsymbol{\pi}^{(4)} = \boldsymbol{\mu}_\pi$. The surrogates are constructed by performing ensembles of meso-

scale reactive void-collapse computations at different values of P_s ranging from 5 through 60 GPa, at 5 GPa intervals. The computations are performed for $D_{void} = 0.5\mu m$ to obtain the deterministic surrogates, denoted by $\dot{F}_{ignition}(P_s; \boldsymbol{\mu_\pi})$ and $\dot{F}_{growth}(P_s; \boldsymbol{\mu_\pi})$.

2. The deterministic surrogates are evaluated at $\hat{P}$ and are combined with the pdfs $\tilde{\dot{F}}_{ignition}(\hat{P})$ and $\tilde{\dot{F}}_{growth}(\hat{P})$ (Section 2.2.3) to define two non-dimensional random variables, $\tilde{\dot{F}}^*_{ignition}$ and $\tilde{\dot{F}}^*_{growth}$:

$$\tilde{\dot{F}}^*_{ignition} = \frac{\tilde{\dot{F}}_{ignition}(\hat{P})}{\dot{F}_{ignition}(P_s = \hat{P}; \boldsymbol{\mu_\pi})} \tag{9a}$$

and

$$\tilde{\dot{F}}^*_{growth} = \frac{\tilde{\dot{F}}_{growth}(\hat{P})}{\dot{F}_{growth}(\hat{P}; \boldsymbol{\mu_\pi})} \tag{9b}$$

The numerators in the above equations are random variables, while the denominators are deterministic scalars, obtained by probing the surrogates $\dot{F}_{ignition}$ and $\dot{F}_{growth}$ of Step 1 at $P_s = \hat{P}$. Thus, in Eqn.(9), the random variables, $\tilde{\dot{F}}^*_{ignition}$ and $\tilde{\dot{F}}^*_{growth}$, have an order of magnitude of 1 and measure the spread of $\tilde{\dot{F}}_{ignition}(\hat{P})$ and $\tilde{\dot{F}}_{growth}(\hat{P})$, arising due to perturbations in $\boldsymbol{\pi}^{(4)}$.

3. In the next step, $\tilde{\dot{F}}^*_{ignition}$ and $\tilde{\dot{F}}^*_{growth}$ are superposed on the deterministic surrogates $\dot{F}_{ignition}(P_s; \boldsymbol{\mu_\pi})$ and $\dot{F}_{growth}(P_s; \boldsymbol{\mu_\pi})$ to obtain the stochastic surrogates $\tilde{\dot{F}}_{ignition}(P_s)$ and $\tilde{\dot{F}}_{growth}(P_s)$ using the following equations.

$$\tilde{\dot{F}}_{ignition}(P_s) = \dot{F}_{ignition}(P_s; \boldsymbol{\mu_\pi}) * \tilde{\dot{F}}^*_{ignition} \tag{10a}$$

and

$$\tilde{\dot{F}}_{growth}(P_s) = \dot{F}_{growth}(P_s; \boldsymbol{\mu_\pi}) * \tilde{\dot{F}}^*_{growth} \tag{10b}$$

In Eqn. (10), the first terms on the RHS are deterministic surrogates, $\dot{F}_{ignition}(P_s; \boldsymbol{\mu_\pi})$ and $\dot{F}_{growth}(P_s; \boldsymbol{\mu_\pi})$ depending only on P_s, while the second terms, $\tilde{\dot{F}}^*_{ignition}$ and $\tilde{\dot{F}}^*_{ignition}$ are random variables, with the randomness resulting from uncertainties in $\boldsymbol{\pi}^{(4)}$. Thus, Eqn. (10) decomposes the random surrogate models $\tilde{\dot{F}}_{ignition}(P_s)$ and $\tilde{\dot{F}}_{growth}(P_s)$ into two independent components – a deterministic pressure dependent term, accounting for the variation of the meso-scale product formation rates due to pressure, and a stochastic modifier, with an order of magnitude of 1, accounting for the perturbation of the surrogate due to variations in material properties at the mesoscale.

4. The $\tilde{\dot{F}}_{ignition}(P_s)$ and $\tilde{\dot{F}}_{growth}(P_s)$ computed using Eqn. (10) are combined with Eqn. (4) to obtain the random macro-scale reaction progress variables, $\tilde{\lambda}_{ignition}(P_s)$ and $\tilde{\lambda}_{growth}(P_s)$, using the following equation.

$$\tilde{\lambda}_{ignition}(P_s) = \phi\tilde{\dot{F}}_{ignition}(P_s); \ \tilde{\lambda}_{growth}(P_s) = \phi\tilde{\dot{F}}_{growth}(P_s) \tag{11}$$

The macro-scale reaction progress variables $\tilde{\lambda}_{ignition}(P_s)$ and $\tilde{\lambda}_{growth}(P_s)$ are used by the macro-scale computational model described in Section 2.1.1 to compute the uncertainties in run-to-detonation distances, h, as discussed next.

2.2.4. Surrogate-based Monte-Carlo method for quantification of uncertainty in h

The stochastic surrogates, $\tilde{\dot{\lambda}}_{ignition}(P_s)$ and $\tilde{\dot{\lambda}}_{growth}(P_s)$ in Eqn. (11) are used to compute the uncertainties in h at the macro-scale. Similar to Section 2.2.2, a Kriging based Monte Carlo method is used to construct pdfs for h using the following procedure:

1. To construct the pdf at a given P_s, first macro-scale computations are performed at different values of $\tilde{\dot{F}}^*_{ignition}$ and $\tilde{\dot{F}}^*_{growth}$, lying in the range $\left[\mu_{\tilde{\dot{F}}^*_{ignition}} - 3\sigma_{\tilde{\dot{F}}^*_{ignition}} \quad \mu_{\tilde{\dot{F}}^*_{growth}} - 3\sigma_{\tilde{\dot{F}}^*_{growth}} \right] < \left[\tilde{\dot{F}}^*_{ignition} \quad \tilde{\dot{F}}^*_{growth} \right] < \left[\mu_{\tilde{\dot{F}}^*_{ignition}} + 3\sigma_{\tilde{\dot{F}}^*_{ignition}} \quad \mu_{\tilde{\dot{F}}^*_{growth}} + 3\sigma_{\tilde{\dot{F}}^*_{growth}} \right]$.

2. The simulations are used to construct a surrogate of h as functions of $\tilde{\dot{F}}^*_{ignition}$ and $\tilde{\dot{F}}^*_{growth}$. Similar to Section 2.2.2, the surrogates are constructed using the DKG method ; the locations for the macroscale computations are chosen using the sequential algorithm of the DKG method . 64 such macro-scale simulations are performed to obtain a converged surrogate of h as functions of $\tilde{\dot{F}}^*_{ignition}$ and $\tilde{\dot{F}}^*_{growth}$.

3. Similar surrogates for h are constructed at different pressures, viz. for $P_s = 10, 12, 15$ and $20\ GPa$. Each of these surrogates are then probed for values of h at k = 10^6 points in the range $\left[\mu_{\tilde{\dot{F}}^*_{ignition}} - 3\sigma_{\tilde{\dot{F}}^*_{ignition}} \quad \mu_{\tilde{\dot{F}}^*_{growth}} - 3\sigma_{\tilde{\dot{F}}^*_{growth}} \right] < \left[\tilde{\dot{F}}^*_{ignition} \quad \tilde{\dot{F}}^*_{growth} \right] < \left[\mu_{\tilde{\dot{F}}^*_{ignition}} + 3\sigma_{\tilde{\dot{F}}^*_{ignition}} \quad \mu_{\tilde{\dot{F}}^*_{growth}} + 3\sigma_{\tilde{\dot{F}}^*_{growth}} \right]$. The probe points are the same as those used for constructing the pdfs, $\tilde{\dot{F}}^*_{ignition}$ and $\tilde{\dot{F}}^*_{growth}$ in Section 2.2.2; the values of these probe points are used to construct the pdfs $\tilde{h}$ at $P_s = 10, 12, 15$ and $20\ GPa$. In addition to the joint pdf, conditional pdfs for the run-to-detonation distances are also constructed to delineate the effects of the individual uncertainties in $\dot{F}_{ignition}$ and $\dot{F}_{growth}$ on h. For example, the conditional pdf $\tilde{h}(\tilde{\dot{F}}_{ignition} | \mu_{\tilde{\dot{F}}^*_{growth}})$ is computed by probing the surrogate for h at k = 10^6 random points in the interval $\left[\mu_{\tilde{\dot{F}}^*_{ignition}} - 3\sigma_{\tilde{\dot{F}}^*_{ignition}} \quad \mu_{\tilde{\dot{F}}^*_{growth}} \right] < \left[\tilde{\dot{F}}^*_{ignition} \quad \tilde{\dot{F}}^*_{growth} \right] < \left[\mu_{\tilde{\dot{F}}^*_{ignition}} + 3\sigma_{\tilde{\dot{F}}^*_{ignition}} \quad \mu_{\tilde{\dot{F}}^*_{growth}} \right]$. The conditional pdf, $\tilde{h}(\tilde{\dot{F}}_{growth} | \mu_{\tilde{\dot{F}}^*_{ignition}})$ is also constructed similarly.

4. The joint pdfs of $\tilde{h}$ at each of the aforementioned pressures are used to compute the equal tail-set 90% confidence interval (CI) of $\tilde{h}$ at $P_s = 10, 12, 15$ and $20\ GPa$. These are then compared against the experimental pop-plot of Vanpoperynghe et al. [18], as reported by Massoni et al. .

Through the above procedures, the pdfs of $\tilde{h}$ reflect the uncertainties in the run-to-detonation distances due to variabilities in the material properties $\boldsymbol{\pi}^{(4)}$ of pressed HMX. Figure 1 shows a summary of the overall procedure for propagating uncertainties from the meso- to the macro-scale. As noted in the figure, the uncertainties in $\boldsymbol{\pi}^{(4)}$ are first used to construct the pdfs of the meso-scale quantities of interest, $\dot{F}_{ignition}$ and $\dot{F}_{growth}$ using the methods described in Section 2.2. These are then used to construct stochastic surrogate models for $\dot{\lambda}_{ignition}(P_s)$ and $\dot{\lambda}_{growth}(P_s)$, as described in Section 2.3. Finally, the stochastic surrogates are used to compute confidence intervals for h (Section 2.4) to determine the uncertainties in the pop-plot for pressed HMX.

3. RESULTS AND DISCUSSION

The methods described in the previous section are used to quantify the uncertainties in h due to variations in $\boldsymbol{\pi}^{(4)}$. The meso-scale computational set-up is shown next and grid convergence results are discussed.

Following this, the pdfs for the meso-scale QoIs, viz. $\tilde{\dot{F}}_{ignition}(\hat{P})$ and $\tilde{\dot{F}}_{growth}(\hat{P})$ are discussed. Finally, the uncertainties in $\tilde{\dot{F}}_{ignition}(\hat{P})$ and $\tilde{\dot{F}}_{growth}(\hat{P})$ are propagated to the macro-scale, and the pdfs for $\tilde{h}$ are shown.

3.1. Meso-scale computations and grid convergence studies

The meso-scale computational set-up for reactive void-collapse is shown in Figure 6a. In the simulations, a void of diameter D_{void} is embedded in a matrix of solid HMX, with dimensions $5D_{void} \times 5D_{void}$. The material is loaded with a rectangular pressure pulse of magnitude P_s and duration τ. Computations are performed to track the evolution of the hot-spots due to void-collapse. The meso-scale product formation rates, $\dot{F}_{ignition}$ and $\dot{F}_{growth}$, are computed from the simulations using the procedure described in Nassar et al .

Figure 6b and c show the rate of convergence of $\dot{F}_{ignition}$ and $\dot{F}_{growth}$ for $P_s = 22\ GPa$ and $D_{void} = 0.5\mu m$ with respect to the grid size, Δx, of the meso-scale computations. As shown in the figure, the variation of $\dot{F}_{ignition}$ and $\dot{F}_{growth}$ is modest for $D_{void}/\Delta x > 600$, i.e. $\dot{F}_{ignition}$ and $\dot{F}_{growth}$ converge to approximately $10^8 s^{-1}$ and $10^9 s^{-1}$ for $D_{void}/\Delta x > 600$. Therefore, in the remaining sections of the report, meso-scale computations are performed for $\Delta x = D_{void}/600$ to quantify the uncertainties in $\dot{F}_{ignition}$ and $\dot{F}_{growth}$ due to variations in $\boldsymbol{\pi}^{(4)}$.

3.2. Quantification of uncertainties in $\dot{F}_{ignition}$ and $\dot{F}_{growth}$

3.2.1. Surrogate models for $\dot{F}_{ignition}$ and $\dot{F}_{growth}$ as functions of C_P, σ_Y, α and BM

As discussed in Section 2.2.2, the uncertainties in $\dot{F}_{ignition}$ and $\dot{F}_{growth}$ are quantified by constructing pdfs for these functions using a surrogate-based Monte-Carlo method. The surrogates for $\dot{F}_{ignition}$ and $\dot{F}_{growth}$ in the $\boldsymbol{\pi}^{(4)}$ parameter space are shown in Figure 4. Because $\boldsymbol{\pi}^{(4)}$ is a four-dimensional vector, the surrogates in Figure 4 are shown as three-dimensional "slices" in the $\boldsymbol{\pi}^{(4)}$ parameter space. Thus, Figure 4a, and b are the surrogates obtained by fixing C_P at 1300 J/KgK (Figure 4a,b). Similarly, surrogates for $C_P = 1800$ J/KgK and 2300 J/KgK are shown in Figure 4c-d and Figure 4e-f respectively.

Figure 4 shows that when C_P is held constant, the variations in $\dot{F}_{ignition}$ and $\dot{F}_{growth}$ in the $\sigma_Y - \alpha - K_T$ parameter space are modest. As seen in Figure 4a, for $C_P = 1300$ J/KgK, $\dot{F}_{ignition}$ varies from $2.1 \times 10^8 s^{-1}$ to $3.0 \times 10^8 s^{-1}$, i.e. $\dot{F}_{ignition}$ varies by 30% in the $\sigma_Y - \alpha - K_T$ space. Similarly, in Figure 4c, $\dot{F}_{ignition}$ varies by 26% for $C_P = 1800$ J/KgK. For higher C_P, such as for $C_P = 2300$ J/KgK in Figure 4e, the percentage is slightly higher, i.e. $\dot{F}_{ignition}$ varies by 63% in the $\sigma_Y - \alpha - K_T$ parameter space. Nevertheless, in the surrogates with constant C_P, the orders of magnitude of $\dot{F}_{ignition}$ remain the same in Figure 4a,c, and e. The same conclusion applies to $\dot{F}_{growth}$; i.e. if C_P is held constant and all the other three parameters, σ_Y, α and K_T, are varied, the orders of magnitude of $\dot{F}_{growth}$ remain the same. Therefore, for a constant C_P, the orders of magnitude of both $\dot{F}_{ignition}$ and $\dot{F}_{growth}$ are not affected by variations in σ_Y, α and K_T.

On the other hand, when C_P is varied, $\dot{F}_{ignition}$ and $\dot{F}_{growth}$ change by an order of magnitude. A comparison of Figure 4a, c and e shows that $\dot{F}_{ignition}$ changes from an order of 10^8 to $10^6 s^{-1}$ when C_P is increased

from 1300 J/KgK to 2300 J/KgK. Similarly, Figure 4b, d and f show that $\dot{F}_{growth}$ changes from an order of 10^9 to $10^7 s^{-1}$ when C_P is increased from 1300 J/KgK to 2300 J/KgK. Therefore, contrary to σ_Y, α or K_T, variations in C_P lead to orders of magnitude variability in $\dot{F}_{ignition}$ and $\dot{F}_{growth}$.

The relative importance of C_P, σ_Y, α and K_T on $\dot{F}_{ignition}$ and $\dot{F}_{growth}$ is further elucidated in the line plots shown in Figure 5. In the figure, three out of the four variables in $\boldsymbol{\pi}_4$ are kept constant at a time and are set to their mean values. For example, for the black line in Figure 5, C_P is allowed to vary, while α, σ_Y and K_T are fixed at μ_α, μ_{σ_Y} and μ_{K_T}. The process is repeated by varying the other three variables in $\boldsymbol{\pi}_4$ one at a time, while fixing the remaining parameters to their mean values. The variations of $\dot{F}_{ignition}$ and $\dot{F}_{growth}$ due to individual variations in C_P, σ_Y, α and K_T are plotted in Figure 5a and b respectively. Figure 5 shows that there is an order of magnitude variation in both $\dot{F}_{ignition}$ and $\dot{F}_{growth}$ when C_P is varied, whereas the variations in $\dot{F}_{ignition}$ and $\dot{F}_{growth}$ due to variations in K_T, σ_Y or α is modest.

3.2.2. Probability density functions for $\dot{F}_{ignition}$ and $\dot{F}_{growth}$

The surrogates in Figure 4 are sampled at the $k = 10^6$ MC points to construct the pdfs, $\tilde{\dot{F}}_{ignition}(\hat{P})$ and $\tilde{\dot{F}}_{growth}(\hat{P})$, which are shown in Figure 7. The figure shows that both $\tilde{\dot{F}}_{ignition}(\hat{P})$ and $\tilde{\dot{F}}_{growth}(\hat{P})$ follow log-normal distributions, i.e.

$$\ln(\tilde{\dot{F}}_{ignition}(\hat{P})\ ) \sim N\left(\mu_{\tilde{\dot{F}}_{ignition}}, \sigma^2_{\tilde{\dot{F}}_{ignition}}\right) \tag{12a}$$

and

$$\ln(\tilde{\dot{F}}_{growth}(\hat{P})) \sim N\left(\mu_{\tilde{\dot{F}}_{growth}}, \sigma^2_{\tilde{\dot{F}}_{growth}}\right) \tag{11b}$$

with mean $\mu_{\tilde{\dot{F}}_{ignition}} = 17.8$, $\mu_{\tilde{\dot{F}}_{growth}} = 19.97$ and the standard deviations $\sigma_{\tilde{\dot{F}}_{ignition}} = 0.34$ and $\sigma_{\tilde{\dot{F}}_{growth}} = 0.3$, i.e. the most probable values of $\tilde{\dot{F}}_{ignition}(\hat{P})$ and $\tilde{\dot{F}}_{growth}(\hat{P})$ are $e^{17.8} \approx 5 \times 10^7 s^{-1}$ and $e^{19.97} \approx 4.7 \times 10^8 s^{-1}$.

It is noted that in Section 2.2.2, $\tilde{\boldsymbol{\pi}}^{(4)}$ was assumed to follow a Normal distribution (Eqn. (8)), i.e. $\tilde{\boldsymbol{\pi}}^{(4)}$ was described by a linear pdf. In contrast, in Figure 7, the pdfs for $\tilde{\dot{F}}_{ignition}(\hat{P})$ and $\tilde{\dot{F}}_{growth}(\hat{P})$ are shown to be logarithmic (Eqn. (10)). Thus, an input uncertainty is exponentially amplified in the meso-scale simulations, resulting in log-normal probability distributions of $\tilde{\dot{F}}_{ignition}(\hat{P})$ and $\tilde{\dot{F}}_{growth}(\hat{P})$.

In addition to the joint pdfs, conditional pdfs for $\tilde{\dot{F}}_{ignition}(\hat{P})$ and $\tilde{\dot{F}}_{growth}(\hat{P})$ are also constructed using the procedures described in Section 2.2.2; the conditional pdfs are shown in Figure 8.

Figure 8a and b show that the conditional pdfs, $\tilde{\dot{F}}_{ignition}(\tilde{C}_P|\mu_\alpha, \mu_{\sigma_Y}, \mu_{K_T})$ and $\tilde{\dot{F}}_{growth}(\tilde{C}_P|\mu_\alpha, \mu_{\sigma_Y}, \mu_{K_T})$, follow log-normal distributions. The means and standard deviations of the log-normal distributions are 17.82 and 0.34 for $\tilde{\dot{F}}_{ignition}(\tilde{C}_P|\mu_\alpha, \mu_{\sigma_Y}, \mu_{K_T})$, while these are 19.96 and 0.3 for $\tilde{\dot{F}}_{growth}(\tilde{C}_P|\mu_\alpha, \mu_{\sigma_Y}, \mu_{K_T})$. Figure 8a and b illustrate two interesting aspects. First, an uncertainty in $\tilde{C}_P$ amplifies exponentially in the

meso-scale model — $\tilde{C}_P$ follows a linear pdf (normal distribution), whereas $\tilde{\tilde{F}}_{ignition}\left(\tilde{C}_P | \mu_\alpha, \mu_{\sigma_Y}, \mu_{K_T}\right)$ and $\tilde{\tilde{F}}_{growth}\left(\tilde{C}_P | \mu_\alpha, \mu_{\sigma_Y}, \mu_{K_T}\right)$ follow log-normal distributions, as shown in Figure 8a and b. Second, a comparison of Figure 8a and b with Figure 7 shows that the means and the standard deviations of the conditionals $\tilde{\tilde{F}}_{ignition}\left(\tilde{C}_P | \mu_\alpha, \mu_{\sigma_Y}, \mu_{K_T}\right)$ and $\tilde{\tilde{F}}_{growth}\left(\tilde{C}_P | \mu_\alpha, \mu_{\sigma_Y}, \mu_{K_T}\right)$ are nearly equal to the means and the standard deviations of the joint pdfs for $\tilde{\tilde{F}}_{ignition}(\hat{P})$ and $\tilde{\tilde{F}}_{growth}(\hat{P})$. For example, the means and standard deviations are 19.96 and 0.3 for the conditional pdf $\tilde{\tilde{F}}_{growth}\left(\tilde{C}_P | \mu_\alpha, \mu_{\sigma_Y}, \mu_{K_T}\right)$, while these are 19.97 and 0.3 for $\tilde{\tilde{F}}_{growth}$. Thus, the joint pdfs $\tilde{\tilde{F}}_{ignition}(\hat{P})$ and $\tilde{\tilde{F}}_{growth}(\hat{P})$ almost overlap with the conditional pdfs $\tilde{\tilde{F}}_{ignition}\left(\tilde{C}_P | \mu_\alpha, \mu_{\sigma_Y}, \mu_{K_T}\right)$ and $\tilde{\tilde{F}}_{growth}\left(\tilde{C}_P | \mu_\alpha, \mu_{\sigma_Y}, \mu_{K_T}\right)$ and the uncertainties in the joint pdfs result primarily from variations in C_P.

In contrast to C_P, Figure 8c and d show that $\tilde{\tilde{F}}_{ignition}$ and $\tilde{\tilde{F}}_{growth}$ are only modestly affected by variabilities in α. $\tilde{\tilde{F}}_{ignition}\left(\tilde{\alpha} | \mu_{C_P}, \mu_{\sigma_Y}, \mu_{K_T}\right)$ follows a multi-modal distribution, and the spread of the pdf is an order of magnitude lower than the mean value of $\tilde{\tilde{F}}_{ignition}$. Similarly, the means and standard deviations of the conditional pdf, $\tilde{\tilde{F}}_{growth}\left(\tilde{\alpha} | \mu_{C_P}, \mu_{\sigma_Y}, \mu_{K_T}\right)$ are respectively $4.8 \times 10^8/s$ and $2.8 \times 10^6/s$, i.e. the spread in the pdf is two orders of magnitude lower than the mean. Similar conclusions also apply to the remaining pdfs, $\tilde{\tilde{F}}_{ignition}\left(\tilde{\sigma}_Y | \mu_{C_P}, \mu_\alpha, \mu_{K_T}\right)$, $\tilde{\tilde{F}}_{ignition}\left(\tilde{K}_T | \mu_{C_P}, \mu_\alpha, \mu_{\sigma_Y}\right)$, $\tilde{\tilde{F}}_{growth}\left(\tilde{\sigma}_Y | \mu_{C_P}, \mu_\alpha, \mu_{K_T}\right)$ and $\tilde{\tilde{F}}_{growth}\left(\tilde{K}_T | \mu_{C_P}, \mu_\alpha, \mu_{\sigma_Y}\right)$, as observed in Figure 8e-h; in each of these cases, the spreads of the pdfs are at least an order of magnitude lesser than the modal values. Therefore, Figure 8 shows that $\tilde{\tilde{F}}_{ignition}$ and $\tilde{\tilde{F}}_{growth}$ are relatively insensitive to variabilities in σ_Y, α and K_T, and the uncertainties in $\tilde{\tilde{F}}_{ignition}$ and $\tilde{\tilde{F}}_{growth}$ result primarily from the uncertainties in C_P. The underlying physics behind these observations is discussed in the following section.

3.2.3. Meso-scale computations for studying the sensitivity of $\tilde{\tilde{F}}_{ignition}$ and $\tilde{\tilde{F}}_{growth}$ with respect to variations in $\boldsymbol{\pi}^{(4)}$

To understand the relative sensitivity of $\dot{F}_{ignition}$ and $\dot{F}_{growth}$ to individual variations in C_P, σ_Y, α and K_T, meso-scale simulations of reactive void-collapse are performed, using the set-up described in Section 3.1. A total of 5 simulations are performed. The first simulation, hereafter referred to as Case A, is performed by setting $\boldsymbol{\pi}^{(4)} = \boldsymbol{\mu}_{\boldsymbol{\pi}}$. In the second case (Case B), σ_Y, α and K_T are maintained at $\mu_\alpha, \mu_{\sigma_Y}, \mu_{K_T}$, while C_P is set to $C_{P,max} = 2300 J/KgK$, which is the maximum value of C_P in Table 1. Similarly, in Cases C, D and E only σ_Y, α or K_T are perturbed from their value in $\boldsymbol{\mu}_{\boldsymbol{\pi}}$ and are set to $\sigma_{Y,max} = 370 MPa$ (Case C), $\alpha_{max} = 27 \times 10^{-5}/K$ (Case D) and $K_{T,max} = 16.4 GPa$ (Case E), while the remaining variables in $\boldsymbol{\pi}^{(4)}$ are maintained at their respective mean values.

Figure 9 shows the temperature contours at 4 stages of void-collapse. As explained in Sen et al. and Nassar et al. , $\dot{F}_{ignition}$ is the slope of the F vs t plot between stages 1 and 2, while $\dot{F}_{growth}$ is the slope of the plot between stages 3 and 4. The plots of the evolution of F, the hot-spot temperature (T_{hs}) and area (A_{hs}) of the hot-spot with time are shown in Figure 10. These figures are used to study the physics behind the relative sensitivity of $\dot{F}_{ignition}$ and $\dot{F}_{growth}$ with respect to C_P, σ_Y, α and K_T.

Effect of C_P: Figure 9a and b show that when C_P is increased from μ_{C_P} to $C_{P,max}$, the hot-spot area is larger but the hot-spot temperature is lower. Thus, increasing C_P results in a larger, but less concentrated hot-spot. Because the hot-spot area is larger, chemical reactions start at a larger fraction of the computational domain for Case B (Figure 9b), compared to Case A (Figure 9a). The reaction adds energy to the system via the source term, $\dot{\mathcal{E}}$, in Eqn. (A3). The larger reaction zone in Case B leads to higher product-mass fraction compared to Case A. Additionally, the source term, $\dot{\mathcal{E}}$, is also proportional to C_P; therefore a higher C_P further aids the process of forming higher product-mass fractions in Case B. Therefore, both $\tilde{F}_{ignition}$ and $\tilde{F}_{growth}$ increase when C_P is increased, as observed in Figure 10a and b.

Effect of σ_Y: A comparison of Figure 9a and c show that the effect of σ_Y is negligible on the evolution of the hot-spot. This is because, for $P_s = 22 GPa$, the melt temperature of HMX (~ 552K) is exceeded even before the collapse of the void is complete, as seen from FigureFigure 9. Once the melt-temperature is exceeded, the deviatoric stresses in the computational terms are set to zero. Thus, the effect of σ_Y on T_{hs}, A_{hs} and F is negligible, as also seen in Figure 10a and c.

Effect of α and K_T : Both α and K_T are used to compute C_v from C_P. Similar to σ_Y, the effect of α as well as K_T on T_{hs}, A_{hs} and F is modest; the contour and the line plots are identical to Figure 9a and are not repeated in the report. The insensitivity of T_{hs}, A_{hs} and F towards α and K_T is because of the fact that in (A9), the second term of the right-hand side is capped off at a maximum value of 200J/KgK. In other words, even when α or K_T are varied by 30% (such as in Cases D and E), their effects are not considered beyond a maximum of 200J/KgK. Therefore, large variations in α or K_T do not affect the meso-scale computations and F is rendered insensitive to variations in α or K_T.

To summarize, $\tilde{F}_{ignition}$ and $\tilde{F}_{growth}$ are only modestly sensitive to σ_Y, α and K_T, whereas the uncertainties in C_P amplify exponentially in the meso-scale computations, resulting in logarithmic pdfs of $\tilde{F}_{ignition}$ and $\tilde{F}_{growth}$. These pdfs are used to propagate the uncertainties in $\boldsymbol{\pi}^{(4)}$ to the macro-scale, as discussed next.

3.3. Uncertainty in the run-to-detonation distance, h

3.3.1.   Uncertainty in the surrogate models for $\dot{F}_{ignition}$ and $\dot{F}_{growth}$

The pdfs for $\tilde{F}_{ignition}(\hat{P})$ and $\tilde{F}_{growth}(\hat{P})$ shown in the previous section are used to construct the stochastic surrogate models, $\tilde{F}_{ignition}(P_s)$ and $\tilde{F}_{growth}(P_s)$, using the methods discussed in 2.2.3. For this, pdfs of the non-dimensional random variables $\tilde{F}^*_{ignition}$ and $\tilde{F}^*_{growth}$ are constructed using Eqn. (9). The pdfs are shown in Figure 11a and b respectively and are found to follow log-normal distributions:

$$\ln(\tilde{F}^*_{ignition}) \sim N\left(\mu_{\tilde{F}^*_{ignition}}, \sigma^2_{\tilde{F}^*_{ignition}}\right) \tag{13a}$$

and

$$\ln(\tilde{F}^*_{growth}) \sim N\left(\mu_{\tilde{F}^*_{growth}}, \sigma^2_{\tilde{F}^*_{growth}}\right) \tag{12b}$$

with $\mu_{\tilde{F}^*_{ignition}} = 0.2$, $\sigma_{\tilde{F}^*_{ignition}} = 0.33$, $\mu_{\tilde{F}^*_{growth}} = 0.15$, and $\sigma_{\tilde{F}^*_{growth}} = 0.3$. The pdfs are the same as those for $\tilde{F}_{ignition}(\hat{P})$ and $\tilde{F}_{growth}(\hat{P})$, except that the order of magnitudes of $\tilde{F}^*_{ignition}$ and $\tilde{F}^*_{growth}$ are

both 1. It is interesting to note in Figure 11a and b that neither $\mu_{\tilde{F}^*_{ignition}}$ nor $\mu_{\tilde{F}^*_{growth}} = 0$, i.e. the means of $\tilde{F}^*_{ignition}$ and $\tilde{F}^*_{growth}$ are not 1. This implies that the mean-values of the pdfs $\tilde{F}_{ignition}(\hat{P})$ and $\tilde{F}_{growth}(\hat{P})$ do not coincide with the values of the deterministic surrogates $\dot{F}_{ignition}(P = \hat{P}; \boldsymbol{\mu_\pi})$ and $\dot{F}_{ignition}(P = \hat{P}; \boldsymbol{\mu_\pi})$, which are evaluated at the mean values of $\tilde{\boldsymbol{\pi}}^{(4)}$. Furthermore, $\mu_{\tilde{F}^*_{ignition}}$ and $\mu_{\tilde{F}^*_{growth}}$ are both positive. Thus, the mean values of the pdfs $\tilde{F}_{ignition}(\hat{P})$ and $\tilde{F}_{growth}(\hat{P})$ are underestimated by the deterministic surrogates $\dot{F}_{ignition}(P_s; \boldsymbol{\mu_\pi})$ and $\dot{F}_{growth}(P_s; \boldsymbol{\mu_\pi})$ evaluated at $P_s = \hat{P}$.

Comparisons of the deterministic surrogates, $\dot{F}_{ignition}(P_s; \boldsymbol{\mu_\pi})$ and $\dot{F}_{growth}(P_s; \boldsymbol{\mu_\pi})$, with the stochastic surrogates $\tilde{F}_{ignition}(P_s)$ and $\tilde{F}_{growth}(P_s)$ are shown in Figure 11c and d. The figures further illustrates the fact that the deterministic surrogates underestimate the mean of the stochastic surrogates. As seen in the figures, the deterministic surrogates lie in the negative 90% confidence interval of $\tilde{F}_{ignition}(P_s)$ and $\tilde{F}_{growth}(P_s)$, i.e. they underestimate the stochastic surrogates. The quantities $\dot{F}_{ignition}$ and $\dot{F}_{ignition}$ measure the energy deposition rate at the meso-scale due to void collapse and hot-spot growth; therefore, Figure 11c and d imply that the deterministic surrogates, $\dot{F}_{ignition}(P_s; \boldsymbol{\mu_\pi})$ and $\dot{F}_{growth}(P_s; \boldsymbol{\mu_\pi})$, underestimate the energy deposition rate at the meso-scale, compared to their stochastic counterparts, $\tilde{F}_{ignition}(P_s)$ and $\tilde{F}_{growth}(P_s)$.

3.3.2. Probability density functions for h and uncertainties in the Pop-plot

To determine the uncertainties in the run-to-detonation distances, pdfs for $\tilde{h}$ are constructed at discrete pressure values of $P_s = 10, 12, 15$ and 20 GPa. The necessary statistics for constructing the pdfs is obtained by sampling surrogate models for h at k Monte-Carlo points (as explained in Section 2.2.4). The surrogates for h are constructed as functions of $\tilde{F}^*_{ignition}$ and $\tilde{F}^*_{growth}$ and are shown in Figure 12(a) through (d) for $P_s = 10, 12, 15$ and 20 GPa respectively. The surrogates show that irrespective of the value of P_s, h is primarily a function of $\tilde{F}^*_{growth}$, and is insensitive to variations in $\tilde{F}^*_{ignition}$. For example, h varies exponentially along the $\tilde{F}^*_{growth}$ axis, but is almost constant along the $\tilde{F}^*_{ignition}$ axis in Figure 12(a). Similar observations can also be made in Figure 12(c)-(d), thereby implying that h is insensitive to $\tilde{F}^*_{ignition}$.

To understand the physics behind the insensitivity of h with respect to $\tilde{F}^*_{ignition}$, three sets of macro-scale computations are performed; in these computations, a 1D coupon of the material is loaded with a sustained shock of $P_s = 15$GPa. In the base case — hereafter referred to as Case A — $\tilde{F}^*_{ignition}$ and $\tilde{F}^*_{growth}$ are set to 1, while in Cases B and C, the values of $[\tilde{F}^*_{ignition}, \tilde{F}^*_{growth}]$ are set to $[1.5, 1]$ and $[1.0, 1.5]$ respectively. In other words, only $\tilde{F}^*_{ignition}$ is perturbed from the base case in Case B, while only $\tilde{F}^*_{growth}$ is perturbed from Case A in Case C.

The evolution of the pressure and the reaction progress variable, λ, for all three cases is shown in Figure 13. A comparison of Figure 13 a and b show that h is insensitive to variabilities in $\tilde{F}^*_{ignition}$. The pressures and λ evolve identically for Cases A and B and h is estimated to be 1.8 mm from the x-t plots in both cases. In contrast, Figure 13c shows that the shock transitions to a detonation faster in Case C, in comparison to Cases A and B. The maximum pressure in the material is attained approximately at 1.5mm, which is also estimated to be the value of h in the x-t plot in the figure. Thus, the simulations confirm that h is primarily

a function of $\tilde{F}^*_{growth}$. This is because, in the MES-IG model, the ignition phase drives the evolution of the reaction-progress variable only initially (until $\lambda = 0.02$), as noted in while Eqn. (2). The majority of the SDT process is governed by the term $\dot{\lambda}_{growth}$, which is a function of $\tilde{F}_{growth}(P_s)$. Therefore, the surrogates of h are insensitive to variabilities in $\tilde{F}^*_{ignition}$ and is primarily a function of $\tilde{F}^*_{growth}$.

The insensitivity of h with respect to $\tilde{F}_{ignition}(P_s)$ can also be observed in Figure 14(a) from the conditional pdf, $\tilde{h}(\tilde{F}_{ignition}|\mu_{\tilde{F}^*_{growth}})$. Figure 14(a) shows that the variations in $\tilde{h}$ in the pdf is always below 0.2 mm for all values of P_s. This implies that the uncertainties in $\tilde{F}_{ignition}$ do not affect the run-to-detonation distances of the material.

Contrary to $\tilde{F}_{ignition}$, variabilities in $\tilde{F}^*_{growth}$ significantly affect h. In Figure 14(c), h is found to vary across orders of magnitude when $\tilde{F}^*_{growth}$ is treated as the random variable and $\tilde{F}^*_{ignition}$ is fixed to $\mu_{\tilde{F}^*_{ignition}}$. In the figure, the conditional pdf $\tilde{h}(\tilde{F}_{growth}|\mu_{\tilde{F}^*_{ignition}})$ is found to follow log-normal distributions. In other words, h varies by orders of magnitude when $\tilde{F}^*_{growth}$ is perturbed.

The stochastic pop-plots, $\tilde{h}$ vs P_s, are shown in Figure 14b and d. In Figure 14b, $\dot{F}_{growth}$ is fixed to a constant value of $\mu_{\tilde{F}^*_{growth}}$, while in Figure 14d, $\dot{F}_{ignition}$ is fixed to a constant value of $\mu_{\tilde{F}^*_{ignition}}$. The figures also compare the stochastic pop-plots with the deterministic pop-plots obtained using the MES-IG model. Both the stochastic and the deterministic predictions are also compared with experimental results.

Three primary observations are made from the pop-plots in Figure 14b and d. First, it is noted that the error bars representing the 90% confidence intervals is negligibly small in Figure 14b, when $\tilde{F}^*_{growth}$ is held constant. This follows from the fact that the uncertainties in $\tilde{F}_{ignition}$ are not propagated to the macro-scale, as discussed earlier. In contrast, the confidence interval in Figure 14d is approximately 90% of the mean value; thus, the variabilities in $\tilde{F}^*_{growth}$ result are propagated to the macro-scale and result in a significant variation in the run-to-detonation distances.

Second, Figure 14b shows that the deterministic h is greater than the mean value of $\tilde{h}$; i.e. deterministic computations predict larger run-to-detonation distances than stochastic computations. This is because the stochastic surrogate model for $\dot{F}_{growth}$ is underestimated by the deterministic model, as discussed in Section 3.3.1. Because $\dot{F}_{growth}$ — the meso-scale energy deposition rate due to void-collapse — is underestimated by the deterministic model, the deterministic h lies in the +90% CI of $\tilde{h}$, as shown in Figure 14d.

Finally, from Figure 14d, it is seen that the experimental observations are in the +90% CI of $\tilde{h}$. Thus, despite the uncertainties in the material properties, the run-to-detonation distances predicted by the MES-IG model are in good agreement with the experimental observations. It is expected that with higher fidelity or improved models of the material properties, $\boldsymbol{\pi}^{(4)}$, the agreement between the computational and the experimental h can be improved even further.

4. CONCLUSIONS

This report quantifies the uncertainty in prediction of the macro-scale QoIs of shock loaded heterogeneous energetic material due to uncertainties in its material properties. The macro-scale QoI, the run-to-detonation distance, is computed using the MES-IG model, which is a multiscale framework for simulating shock to

detonation transitions in energetic materials. The input uncertainties are first used to compute the uncertainties in the meso-scale reaction-product formation rates, $\dot{F}_{ignition}$ and $\dot{F}_{growth}$. To this end, ensembles of reactive void-collapse computations are performed at the meso-scale and pdfs of $\dot{F}_{ignition}$ and $\dot{F}_{growth}$ are constructed. These pdfs are propagated to the macro-scale via surrogate models for $\dot{F}_{ignition}$ and $\dot{F}_{growth}$. These stochastic surrogates are used as inputs to a homogenized macro-scale computational model to determine uncertainties in the macro-scale QoI.

The current work shows that among the six properties considered in this study, viz. $C_p, K_T, \sigma_Y, \alpha, \Gamma, k$, it is the uncertainties in C_p that amplify exponentially across scales, resulting in logarithmic pdfs for $\dot{F}_{ignition}$ and $\dot{F}_{growth}$. However, the uncertainties in $\dot{F}_{ignition}$ are not propagated to the macro-scale QoI, h. In fact, it is only the uncertainties in $\dot{F}_{growth}$ that result in orders of magnitude variations in h. It is further shown that inspite of the uncertainties in the material properties, the experimental h lies in the 90% CI range of the run-to-detonation distances predicted by the MES-IG model. The agreement is expected to increase further with improved estimates of C_p.

Several extensions of the current work are being pursued. First, at low pressures, the yield strength, σ_Y, plays an important role in the formation of hot-spots [Rai and Udaykumar, Austin], and is expected to have significant effects on h. The effects of uncertainties of σ_Y on h at lower pressures is being investigated. Second, the effects of uncertainties due to the microstructural features and the reaction models are also being investigated. In conclusion, the UQ framework presented in this report not only propagates uncertainties across scales is multiscale models of SDT, but also allows to rank the properties with respect to the sensitivity of the SDT response of HE materials on the uncertainty of each property.

REFERENCES

1. Patrone, P., A. Kearsley, and A. Dienstfrey. *The role of data analysis in uncertainty quantification: case studies for materials modeling*. in *2018 AIAA Non-Deterministic Approaches Conference*. 2018.
2. Panchal, J.H., S.R. Kalidindi, and D.L. McDowell, *Key computational modeling issues in integrated computational materials engineering.* Computer-Aided Design, 2013. **45**(1): p. 4-25.
3. Chernatynskiy, A., S.R. Phillpot, and R. LeSar, *Uncertainty quantification in multiscale simulation of materials: A prospective.* Annual Review of Materials Research, 2013. **43**: p. 157-182.
4. Najm, H.N., *Uncertainty quantification and polynomial chaos techniques in computational fluid dynamics.* Annual review of fluid mechanics, 2009. **41**: p. 35-52.
5. Miller, K., S. Berg, J. Davison, E. Sudicky, and P. Forsyth, *Efficient uncertainty quantification in fully-integrated surface and subsurface hydrologic simulations.* Advances in Water Resources, 2018. **111**: p. 381-394.
6. Liu, Y., N. Dinh, and R. Smith, *A Validation and Uncertainty Quantification Framework for Eulerian-Eulerian Two-Fluid Model based Multiphase-CFD Solver. Part I: Methodology.* arXiv preprint arXiv:1806.03373, 2018.
7. Akiki, M., T. Gallagher, G. Hannebique, and S. Menon. *Uncertainty Quantification in the Simulation of Explosive Particle Dispersal using an Eulerian/Lagrangian Formulation*. in *55th AIAA Aerospace Sciences Meeting*. 2017.
8. Brundage, A.L. *Modeling Compressive Reaction in Shock-Driven Secondary Granular Explosives*. in *ASME/JSME 2011 8th Thermal Engineering Joint Conference*. 2011. American Society of Mechanical Engineers.
9. Miao, Z. and Y. Xin, *Application of Quantification of Uncertainties Method in Detonation Simulation to Steven Test.* Procedia Engineering, 2016. **157**: p. 382-386.

10. Tanasoiu, B. and M. Koslowski, *A parametric study of the dynamic failure of energetic composites.* Journal of Applied Physics, 2017. **122**(12): p. 125103.

11. Ramprasad, R., R. Batra, G. Pilania, A. Mannodi-Kanakkithodi, and C. Kim, *Machine learning in materials informatics: recent applications and prospects.* npj Computational Materials, 2017. **3**(1): p. 54.

12. Elton, D.C., Z. Boukouvalas, M.S. Butrico, M.D. Fuge, and P.W. Chung, *Applying machine learning techniques to predict the properties of energetic materials.* arXiv preprint arXiv:1801.04900, 2018.

13. Elkhodary, K.I., M.S. Greene, S. Tang, T. Belytschko, and W.K. Liu, *Archetype-blending continuum theory.* Computer Methods in Applied Mechanics and Engineering, 2013. **254**: p. 309-333.

14. Sen, O., S. Davis, G. Jacobs, and H.S. Udaykumar, *Evaluation of convergence behavior of metamodeling techniques for bridging scales in multi-scale multimaterial simulation.* Journal of Computational Physics, 2015. **294**: p. 585-604.

15. Rai, N.K., M.J. Schmidt, and H. Udaykumar, *High-resolution simulations of cylindrical void collapse in energetic materials: Effect of primary and secondary collapse on initiation thresholds.* Physical Review Fluids, 2017. **2**(4): p. 043202.

16. Tarver, C.M., S.K. Chidester, and A.L. Nichols, *Critical conditions for impact-and shock-induced hot spots in solid explosives.* The Journal of Physical Chemistry, 1996. **100**(14): p. 5794-5799.

17. Massoni, J., R. Saurel, G. Baudin, and G. Demol, *A mechanistic model for shock initiation of solid explosives.* Physics of Fluids (1994-present), 1999. **11**(3): p. 710-736.

18. Vanpoperynghe, J., J. Sorel, J. Aveille, and J. Adenis. *Shock initiation of TATB and HMX explosive compositions.* in *8th Symposium (International) on Detonation.* 1985.

19. Augspurger, M., K. Choi, and H. Udaykumar, *Optimizing fin design for a PCM-based thermal storage device using dynamic Kriging.* International Journal of Heat and Mass Transfer, 2018. **121**: p. 290-308.

20. Menikoff, R. and T.D. Sewell, *Constituent properties of HMX needed for mesoscale simulations.* Combustion theory and modelling, 2002. **6**(1): p. 103-125.

21. Long, Y. and J. Chen, *Theoretical study of the thermodynamic properties, phase transition wave, and phase transition velocity for octahydro-1, 3, 5, 7-tetranitro-1, 3, 5, 7-tetrazocine.* Journal of Applied Physics, 2015. **118**(11): p. 115901.

22. Koshigoe, L., R. Shoemaker, and E. TAYLOR, *Specific heat of HMX.* AIAA journal, 1984. **22**(11): p. 1600-1601.

23. Hanson-Parr, D.M. and T.P. Parr, *Thermal properties measurements of solid rocket propellant oxidizers and binder materials as a function of temperature.* Journal of energetic materials, 1999. **17**(1): p. 1-48.

24. Peng, Q., G. Wang, G.-R. Liu, S. Grimme, and S. De, *Predicting Elastic Properties of β-HMX from First-principles calculations.* The Journal of Physical Chemistry B, 2015. **119**(18): p. 5896-5903.

25. Sewell, T.D., R. Menikoff, D. Bedrov, and G.D. Smith, *A molecular dynamics simulation study of elastic properties of HMX.* The Journal of chemical physics, 2003. **119**(14): p. 7417-7426.

26. Zaug, J.M., *Elastic constants of b-HMX and tantalum, equations of state of supercritical fluids and fluid mixtures and thermal transport determinations.* 1998, Lawrence Livermore National Lab., CA (US).

27. Stevens, L.L. and C.J. Eckhardt, *The elastic constants and related properties of β-HMX determined by Brillouin scattering.* The Journal of chemical physics, 2005. **122**(17): p. 174701.

28. Sun, B., J. Winey, Y. Gupta, and D. Hooks, *Determination of second-order elastic constants of cyclotetramethylene tetranitramine (β-HMX) using impulsive stimulated thermal scattering.* Journal of Applied Physics, 2009. **106**(5): p. 053505.

29. Cui, H.-L., G.-F. Ji, X.-R. Chen, W.-H. Zhu, F. Zhao, Y. Wen, and D.-Q. Wei, *First-principles study of high-pressure behavior of solid β-HMX.* The Journal of Physical Chemistry A, 2009. **114**(2): p. 1082-1092.

30. Han, G., R.-j. Gou, S.-h. Zhang, C.-l. Wu, and S.-f. Zhu, *Theoretical investigation into the influence of molar ratio on binding energy, mechanical property and detonation performance of 1, 3, 5, 7-tetranitro-1, 3, 5, 7-tetrazacyclo octane (HMX)/1-methyl-4, 5-dinitroimidazole (MDNI) cocrystal explosive.* Computational and Theoretical Chemistry, 2017. **1109**: p. 27-35.

31. Xiao, J., G. Fang, G. Ji, and H. Xiao, *Simulation investigations in the binding energy and mechanical properties of HMX-based polymer-bonded explosives.* Chinese Science Bulletin, 2005. **50**(1): p. 21-26.

32. Olinger, B., B. Roof, and H. Cady. *The linear and volume compression of b-HMX and RDX.* in *Proc. Symposium (Intern.) on High Dynamic Pressures.* 1978.

33. Zhang, J., T.L. Jackson, J.D. Buckmaster, and J.B. Freund, *Numerical modeling of shock-to-detonation transition in energetic materials.* Combustion and Flame, 2012. **159**(4): p. 1769-1778.

34. Simo, J. and T. Hughes, *General return mapping algorithms for rate-independent plasticity.* Constitutive laws for engineering materials: theory and applications, 1987. **1**: p. 221-232.

35. Menikoff, R., J. Dick, and D. Hooks, *Analysis of wave profiles for single-crystal cyclotetramethylene tetranitramine.* Journal of applied physics, 2005. **97**(2): p. 023529.
36. Mohan, V.K. and J. Field, *Impact initiation of hexanitrostilbene.* Combustion and flame, 1984. **56**(3): p. 269-277.
37. Zamiri, A.R. and S. De, *Modeling the Anisotropic Deformation Response of β-HMX Molecular Crystals.* Propellants, Explosives, Pyrotechnics, 2011. **36**(3): p. 247-251.
38. Gilbert, J., S. Chakravarthy, and K.A. Gonthier, *Computational analysis of hot-spot formation by quasi-steady deformation waves in porous explosive.* Journal of Applied Physics, 2013. **113**(19): p. 194901.
39. Dong, H., R. Hu, P. Yao, and X. Zhang, *Thermograms of energetic materials.* Natl. Def. Ind. Press, Beijing, 2002: p. 276-300.
40. Data, L.E.P., *TR Gibbs and A. Popolato.* University of California, Berkeley, 1980.
41. Long, Y., J. Chen, Y. Liu, F. Nie, and J. Sun, *A direct method to calculate thermal conductivity and its application in solid HMX.* Journal of Physics: Condensed Matter, 2010. **22**(18): p. 185404.
42. Bedrov, D., G.D. Smith, and T.D. Sewell, *Thermal conductivity of liquid octahydro-1, 3, 5, 7-tetranitro-1, 3, 5, 7-tetrazocine (HMX) from molecular dynamics simulations.* Chemical Physics Letters, 2000. **324**(1-3): p. 64-68.
43. Gump, J. *High-pressure and temperature investigations of energetic materials.* in *Journal of Physics: Conference Series.* 2014. IOP Publishing.
44. Saw, C.K., *Kinetics of HMX and phase transitions: effects of grain size at elevated temperature.* 2002, Lawrence Livermore National Lab., CA (US).
45. Kapahi, A. and H. Udaykumar, *Three-dimensional simulations of dynamics of void collapse in energetic materials.* Shock Waves, 2015. **25**(2): p. 177-187.
46. Kapahi, A. and H.S. Udaykumar, *Dynamics of void collapse in shocked energetic materials: physics of void–void interactions.* Shock Waves, 2013. **23**(6): p. 537-558.
47. Rai, N.K., M. Schmidt, and H.S. UdayKumar, *High Resolution Simulations of Void Collapse in energetic materials: Effect of primary and secondary collapse on initiation thresholds.* Phyiscal Review Fluids. **2**(4): p. 043202.
48. Rai, N.K., M. Schmidt, and H.S. UdayKumar, *Collapse of Elonagted Voids in porous Energetic Materials: Effect of void orientation and aspect ratio on initiation.* Physical Review Fluids. **2**(4): p. 043201.
49. Rai, N.K. and H. Udaykumar, *Three-dimensional simulations of void collapse in energetic materials.* Physical Review Fluids, 2018. **3**(3): p. 033201.
50. Rai, N.K. and H.S. Udaykumar, *Mesoscale simulation of reactive pressed energetic materials under shock loading.* Journal of Applied Physics, 2015. **118**(24): p. 245905.
51. Kapahi, A., J. Mousel, S. Sambasivan, and H. Udaykumar, *Parallel, sharp interface Eulerian approach to high-speed multi-material flows.* Computers & Fluids, 2013. **83**: p. 144-156.
52. Rai, N.K., A. Kapahi, and H.S. Udaykumar, *Treatment of contact separation in Eulerian high-speed multimaterial dynamic simulations.* International Journal for Numerical Methods in Engineering, 2014. **100**(11): p. 793-813.
53. Sambasivan, S., A. Kapahi, and H.S. Udaykumar, *Simulation of high speed impact, penetration and fragmentation problems on locally refined Cartesian grids.* Journal of Computational Physics, 2012.
54. Ponthot, J.-P., *Unified stress update algorithms for the numerical simulation of large deformation elasto-plastic and elasto-viscoplastic processes.* International Journal of Plasticity, 2002. **18**(1): p. 91-126.
55. Kapahi, A., S. Sambasivan, and H. Udaykumar, *A three-dimensional sharp interface Cartesian grid method for solving high speed multi-material impact, penetration and fragmentation problems.* Journal of Computational Physics, 2013. **241**: p. 308-332.
56. Sewell, T.D. and R. Menikoff. *COMPLETE EQUATION OF STATE FOR/3-HMX AND IMPLICATIONS FOR INITIATION.* 2003. American Institute of Physics.
57. Strang, G., *On the construction and comparison of difference schemes.* SIAM Journal on Numerical Analysis, 1968. **5**(3): p. 506-517.
58. Rai, N.K., M.J. Schmidt, and H.S. Udaykumar, *High-resolution simulations of cylindrical void collapse in energetic materials: Effect of primary and secondary collapse on initiation thresholds.* Physical Review Fluids, 2017. **2**(4).
59. Lee, E.L. and C.M. Tarver, *Phenomenological model of shock initiation in heterogeneous explosives.* Physics of Fluids (1958-1988), 1980. **23**(12): p. 2362-2372.
60. Kapila, A., D. Schwendeman, J. Bdzil, and W. Henshaw, *A study of detonation diffraction in the ignition-and-growth model.* Combustion Theory and Modelling, 2007. **11**(5): p. 781-822.
61. Springer, H.K., C.M. Tarver, and S. Bastea, *Effects of High Shock Pressures and Pore Morphology.* 2015.

APPENDIX : THE MES-IG MODEL FOR MULTISCALE MODELING OF SDT IN ENERGETIC MATERIALS

The conservation laws for mass, momentum and energy that apply at both meso- and the macro-scales in the MES-IG model are cast in Eulerian form, viz.:

$$\frac{\partial \rho}{\partial t} + \frac{\partial (\rho u_i)}{\partial x_i} = 0 \tag{A1}$$

$$\frac{\partial (\rho u_i)}{\partial t} + \frac{\partial (\rho u_i u_j - \sigma_{ij})}{\partial x_j} = 0 \tag{A2}$$

and

$$\frac{\partial (\rho E)}{\partial t} + \frac{\partial (\rho E u_j + \sigma_{ij} u_i)}{\partial x_j} = \dot{\mathcal{E}} \tag{A3}$$

where ρ, and u_i, respectively denote the density, and the velocity components, $E = e + \frac{1}{2} u_i u_i$ is the specific total energy, and e is the specific internal energy. The source term $\dot{\mathcal{E}}$ in Eqn. (A3) is the rise in specific internal energy of the system due to heat released in the decomposition of solid HMX into gaseous reaction products. The Cauchy stress tensor, σ_{ij} is of the form:

$$\sigma_{ij} = S_{ij} - p\delta_{ij} \tag{A4}$$

where S_{ij} is the deviatoric stress tensor and p is the pressure.

At the meso-scale, in the high-resolution reactive void collapse calculations performed in the setup shown in Figure 1, the HMX and void spaces are delineated using a sharp-interface Eulerian framework presented in previous work [45-50]. The collapse of voids due to shock loading and the formation of hot spots are modeled with the solid HMX modeled as an elasto-plastic material of constantyield strength, σ_y. Shock heating can lead to the melting of HMX; therefore, thermal softening of HMX is modeled using the Kraut-Kennedy relation [20]. The pressure at the meso-scale is obtained from a Birch-Murnaghan equation of state [20, 56]:

$$p(\rho, e) = p_k(\rho) + \rho \Gamma [e - e_k(\rho)] \tag{A5}$$

where

$$p_k(\rho) = \frac{3}{2} K_{T0} \left[\left(\frac{\rho}{\rho_0} \right)^{7/3} - \left(\frac{\rho}{\rho_0} \right)^{5/3} \right] \left[1 + \frac{3}{4} (K'_{T0} - 4) \left[\left(\frac{\rho}{\rho_0} \right)^{2/3} - 1 \right] \right] \tag{A6}$$

$$e_k(\rho) = e_0 - \int_{1/\rho_0}^{1/\rho} p_k(\rho) \, d\left(\frac{1}{\rho} \right) \tag{A7}$$

and

$$e = e_k(\rho) + C_v T \tag{A8}$$

where Γ is the Gruneisen co-efficient, and T is the temperature. The isochoric specific heat C_v is computed from the isobaric specific heat C_p using the following equation:

$$C_v = C_p - \max(\alpha^2 TVK_T, 200J/KgK) \tag{A9}$$

where α is the thermal expansion co-efficient, and K_T is the bulk modulus.

Chemical decomposition of HMX is modeled in the Tarver 3-equation model [16] via four different species, Y_1 through Y_4. The change in temperature due to chemical decomposition of HMX is calculated by solving the evolution equation,

$$\rho C_p \dot{T} = \dot{Q}_R + k\nabla^2 T \tag{A10}$$

where k is the thermal conductivity of HMX and $\dot{Q}_R$ is the total heat release rate because of the chemical reaction. The source term in Eqn. (A3) is computed by setting $\dot{\mathcal{E}} = C_v \dot{T}$.

At the macro-scale, the material is considered to be a homogenized mixture of solid HMX and gaseous reaction products. The mixture is assumed to behave hydro-dynamically [59, 60], i.e. S_{ij} is neglected in comparison to $p\delta_{ij}$ in Eqn. (A4). The chemical heat release due to the decomposition of HMX into gaseous products is accounted for by transitioning the mixture from a cold, unreacted solid Hugoniot to a product Hugoniot. The equations of state for the reactants and the products are given by a Cochran-Chan and a JWL equation of state, as described in Sen et al.

TABLES

Table 1 Summary of the maximum and minimum values of the material parameters π_i of solid HMX

Parameter, π_i	Minimum	Maximum
Specific Heat (C_p)	1300 J/KgK	2300 J/KgK
Bulk Modulus (K_T)	5.31 GPa [30]	16.4 GPa [24]
Grüneisen Coefficient (γ)	0.7 [33]	1.1 [20]
Yield Strength (Y)	$0.13\ GPa$ [36]	$0.37\ GPa$ [38]
Thermal Conductivity (K_{TH})	$0.29\ W/mK$ [39]	$0.65\ W/mK$ [41]
Thermal Expansion (α_{TH})	$13.1 \times 10^{-5}/K$ [20]	$27.0 \times 10^{-5}/K$ [43]

Table 2. The mean μ_π and the standard deviation σ_π in the probability density function for $\tilde{\pi}$

	$\alpha\ (\times 10^{-5}/K)$	$Y\ (GPa)$	$K_T\ (GPa)$	$C_p\ (J\ kg^{-1}K^{-1})$
Mean	20.05	0.249	10.8545	1800
Standard Deviation	1.39	0.0242	1.1091	100

FIGURES
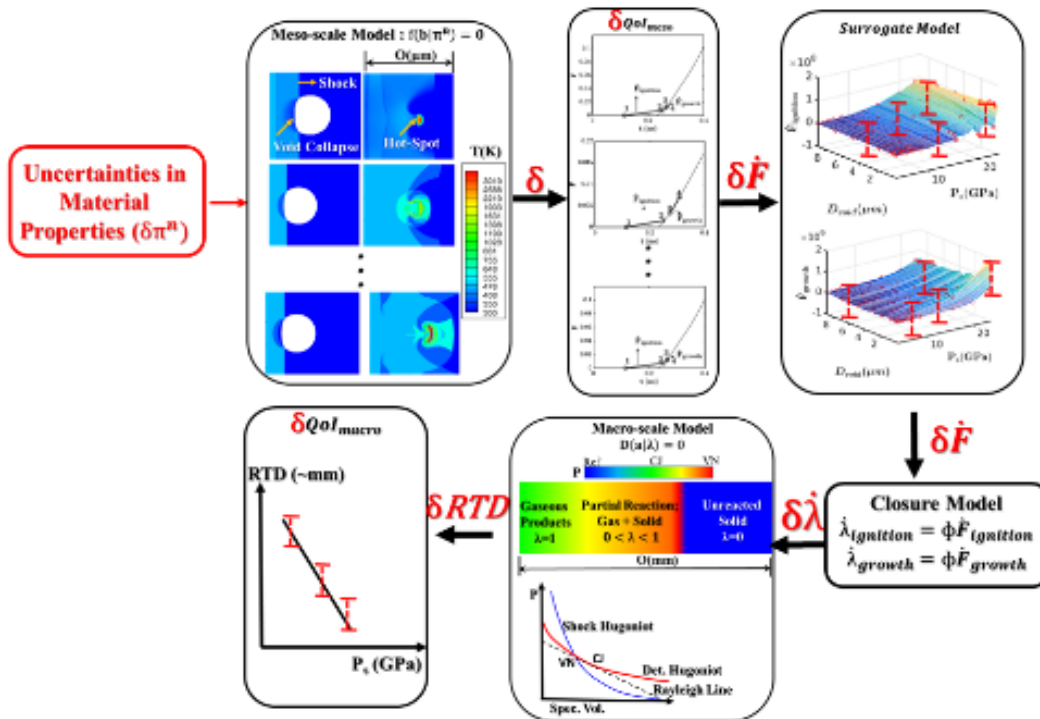
Figure 1. Schematic representation of uncertainty propagation across scales in the MES-IG model. The MES-IG model performs ensembles of high-fidelity meso-scale reactive void-collapse computations to compute two meso-scale product formations rates, $\dot{F}_{ignition}$ and $\dot{F}_{growth}$. These are then used as inputs to a Kriging method to constructs surrogates of the form $\dot{F}_{ignition}(P_s, D_{void})$ and $\dot{F}_{growth}(P_s, D_{void})$. The surrogates are used to compute the macro-scale reaction progress variables, $\dot{\lambda}_{ignition}$ and $\dot{\lambda}_{growth}$, which are used close a homogenized macro-scale computational model. Macro-scale computations are used to simulate SDT and compute the run-to-detonation distances (RTD) for different shock pressures. The uncertainties (symbolically denoted by δ) in material properties are propagated through the meso-scale computations, resulting in stochastic surrogate models, $\delta\dot{F}_{ignition}(P_s, D_{void})$ and $\delta\dot{F}_{growth}(P_s, D_{void})$. These result in stochastic closure models, $\delta\dot{\lambda}_{ignition}$ and $\delta\dot{\lambda}_{growth}$ for the reaction progress variables, which are fed as inputs to the macro-scale computations. Subsequently, this results in uncertainties in the run-to-detonation distances for the energetic material and are shown as error-bars in the pop-plots.
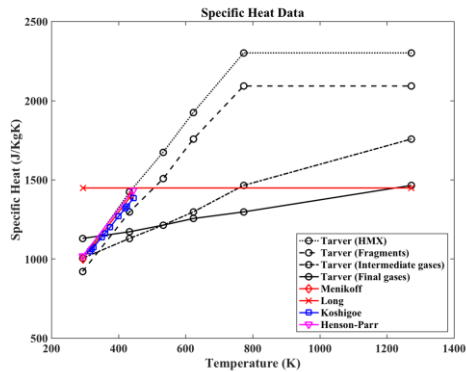
(a)
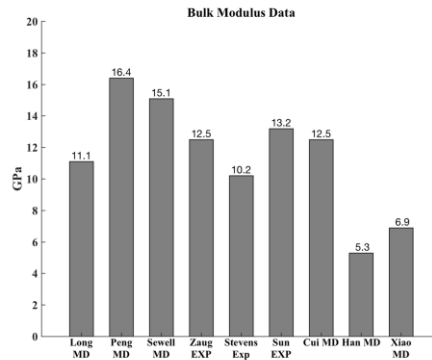
(b)
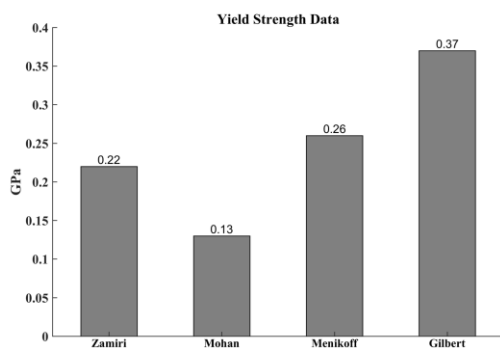
(c)
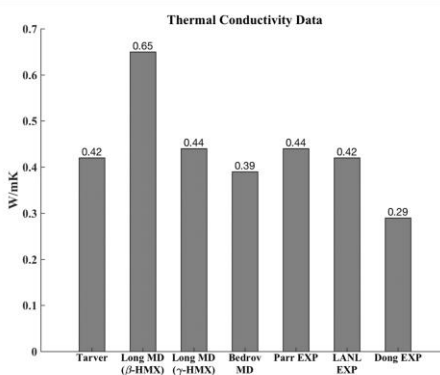
(d)
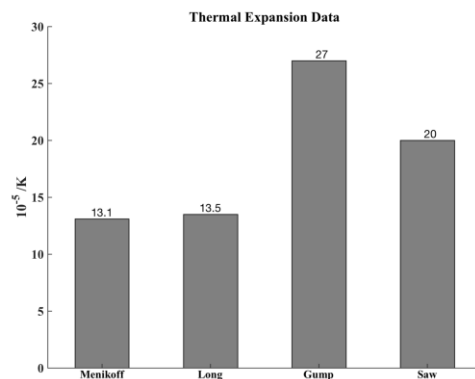
(e)

Figure 2 (a) Distribution of C_P for HMX based on the references [9, 12, 16, 19, 22]. (b) K_T distribution for HMX based on the references [1-9]. MD denotes data estimated by Molecular Dynamics computations while EXP denotes data estimated from experiments. (c) σ_Y distribution for HMX based on the references [10-13]. (d) k distribution of HMX based on the references [16-21]. MD denotes data estimated by Molecular Dynamics computations while EXP denotes data estimated from experiments. (e) α distribution for HMX based on the references [9, 12, 14, 15].
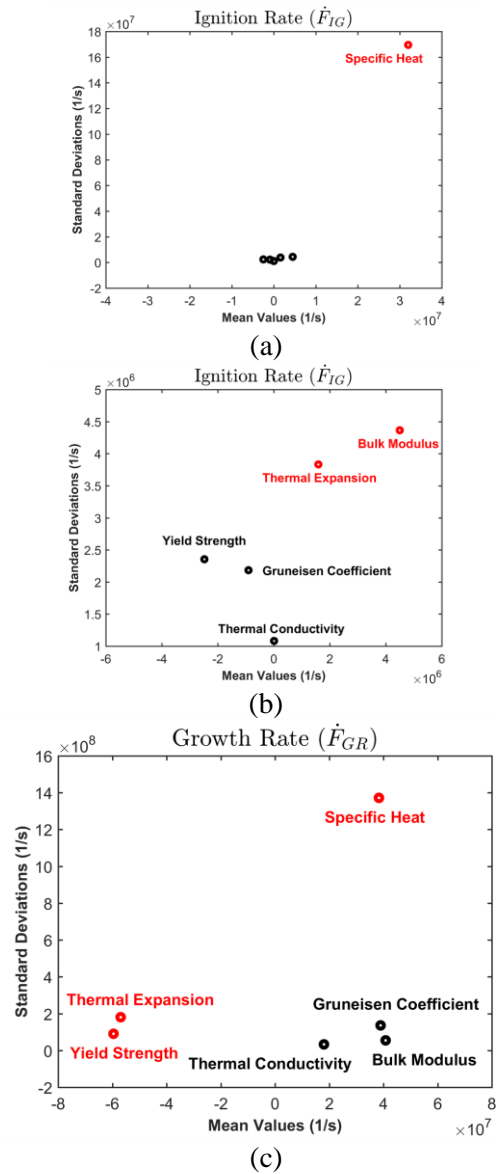
Figure 3 : Elementary screening effects of π_6 on (a)-(b) $\dot{F}_{ignition}$ and (c) $\dot{F}_{growth}$. A high absolute value of the mean of the elementary effects of a variable in π_6 implies that $\dot{F}_{ignition}$ and/or $\dot{F}_{growth}$ is most sensitive to that variable. The mean and the standard deviations of the elementary effects are computed from 4 random orienations.
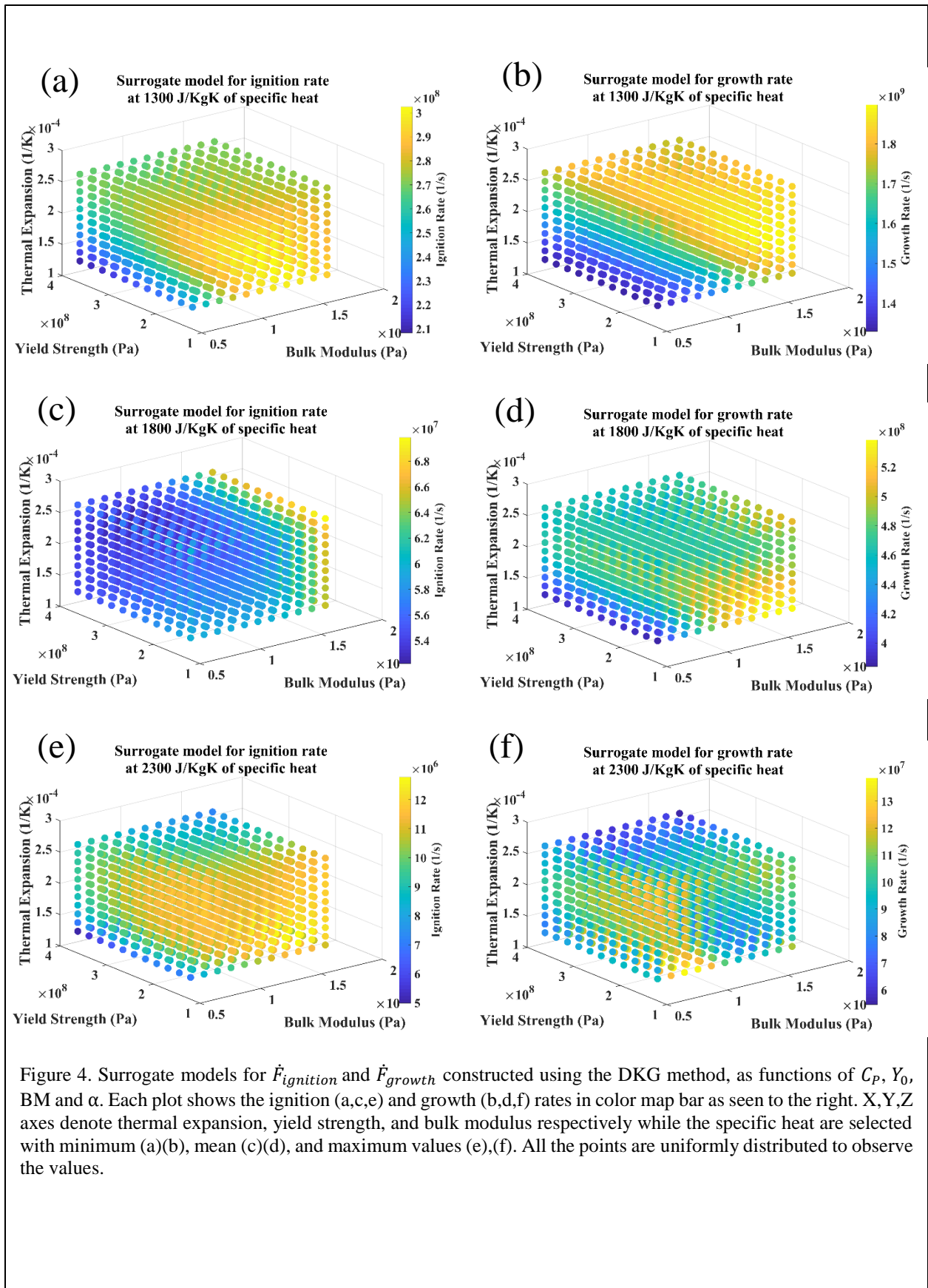
Figure 4. Surrogate models for $\dot{F}_{ignition}$ and $\dot{F}_{growth}$ constructed using the DKG method, as functions of C_P, Y_0, BM and α. Each plot shows the ignition (a,c,e) and growth (b,d,f) rates in color map bar as seen to the right. X,Y,Z axes denote thermal expansion, yield strength, and bulk modulus respectively while the specific heat are selected with minimum (a)(b), mean (c)(d), and maximum values (e),(f). All the points are uniformly distributed to observe the values.
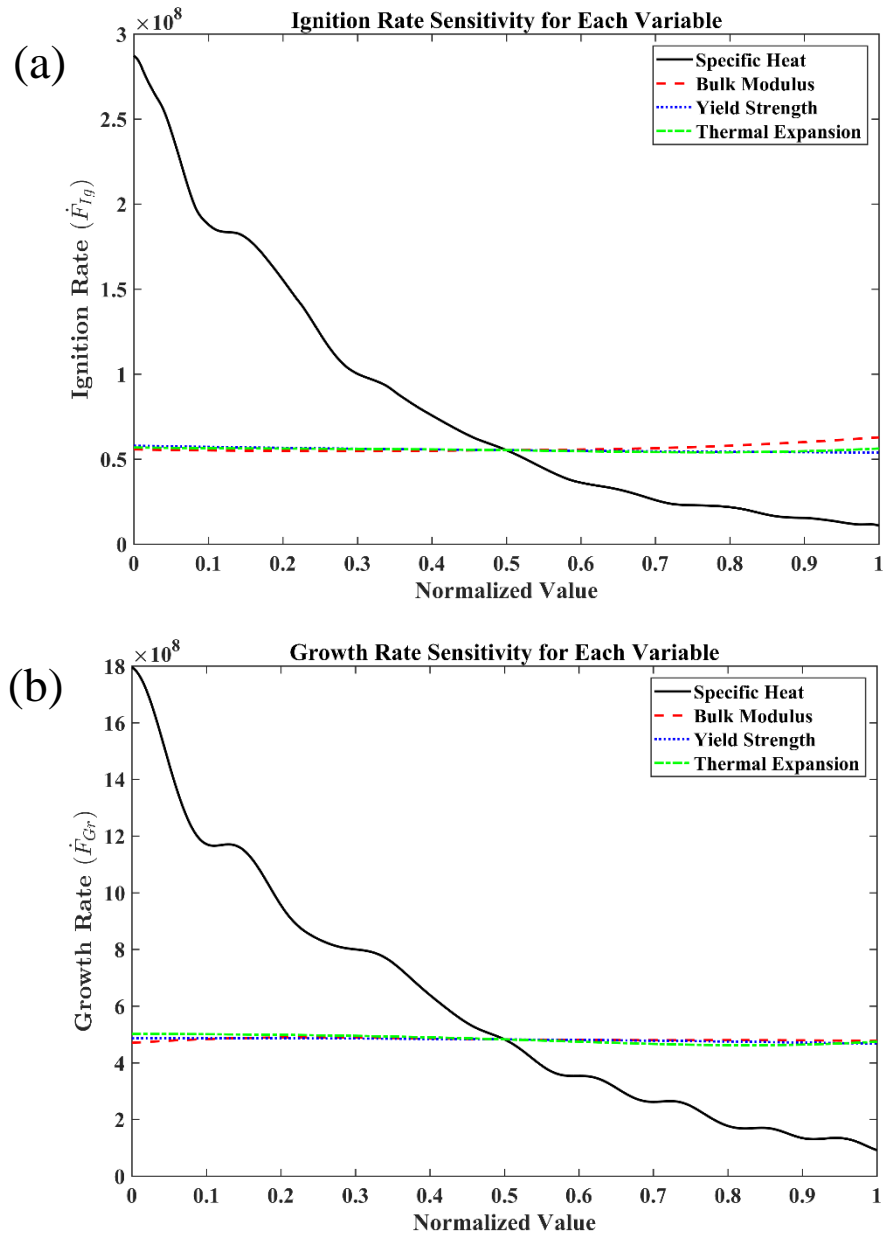
Figure 5. The sensitivity distributions for the (a) ignition and (b) growth rates depending on the parameters of interest in the surrogate models. Other than Fig. 12., the plots show the effects of each parameter of interest. As one parameter is solely considered for the sensitivity analysis, other parameters are all set to their mean values with the boundaries. All the sampling boundaries for each parameter are normalized to compare all in a figure. As seen in the both plots, the ignition and growth rates decrease as specific heat values increase. Compared to the effects of specific heat, other three variables have small variances to the rates so that they even seem close to constant values.

(a)

(b)

(c)
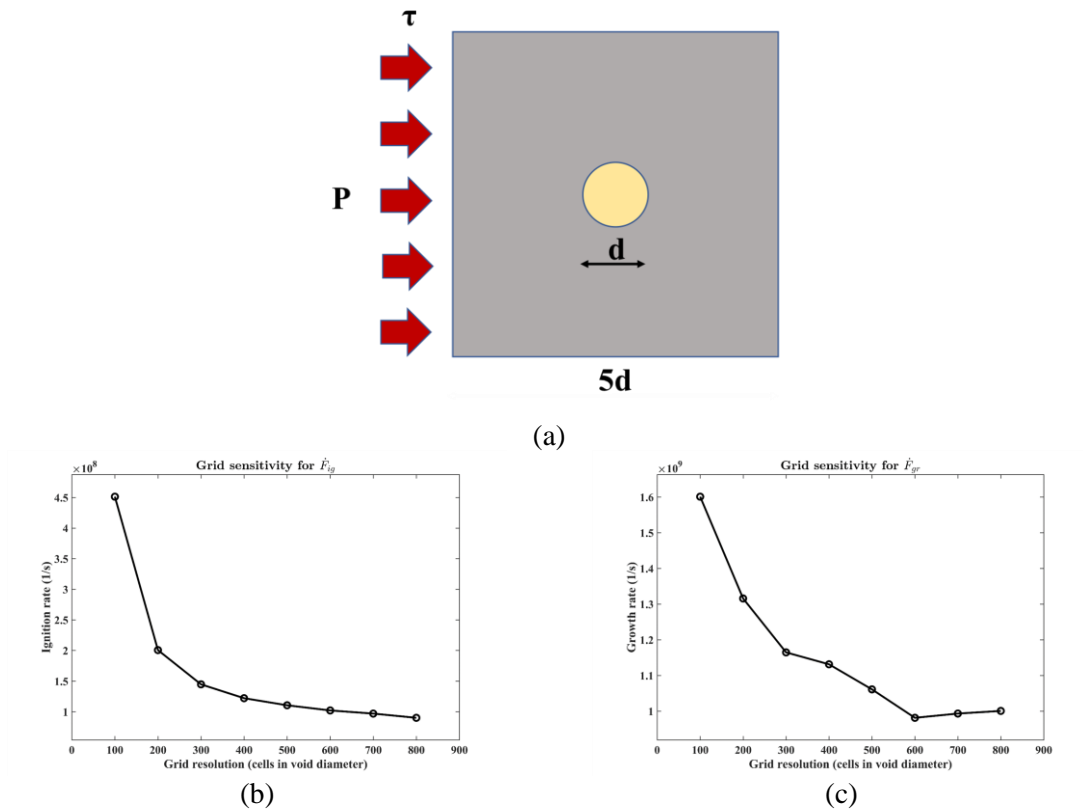
Figure 6 (a) The meso-scale computational set-up for performing reactive void-collapse simulations. A void of diameter $D_{void} = 0.5\mu m$ embedded in solid HMX. The dimensions of the computational domain is $5*D_{void}$ x $5*D_{void}$. The material is loaded with a pressure pulse of strength P_s and duration τ from the west boundary. Computations are performed to obtain $\dot{F}_{ignition}$ and $\dot{F}_{growth}$ from the meso-scale simulations. Figures (b) and (c) show the results of the mesh-refinement study for $\dot{F}_{ignition}$ and $\dot{F}_{growth}$ respectively. The x-axis of the plots represent $D_{void}/\Delta x$, where Δx is the size of the mesh used in the meso-scale computations.
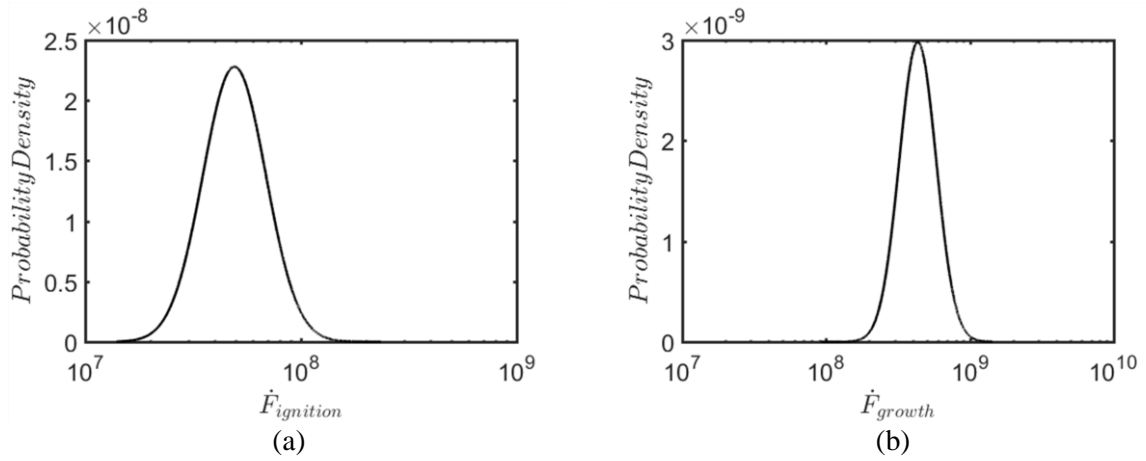
Figure 7. Probability density functions for (a) $\dot{F}_{ignition}$ and (b) $\dot{F}_{growth}$ computed at $P_s = 22\ GPa$ for the collapse of a single isolated cylindrical void of diameter $D_{void} = 0.5\mu m$. The pdfs are constructed by sampling the surrogate for $\dot{F}_{ignition}$ and $\dot{F}_{growth}$ at 1 million sampling points. The pdfs follow a log-normal distribution with mean and variances $\mu_{\dot{F}_{ignition}}, \sigma^2_{\dot{F}_{ignition}}$ for $\dot{F}_{ignition}$ and $\mu_{\dot{F}_{growth}}, \sigma^2_{\dot{F}_{growth}}$ for $\dot{F}_{growth}$.
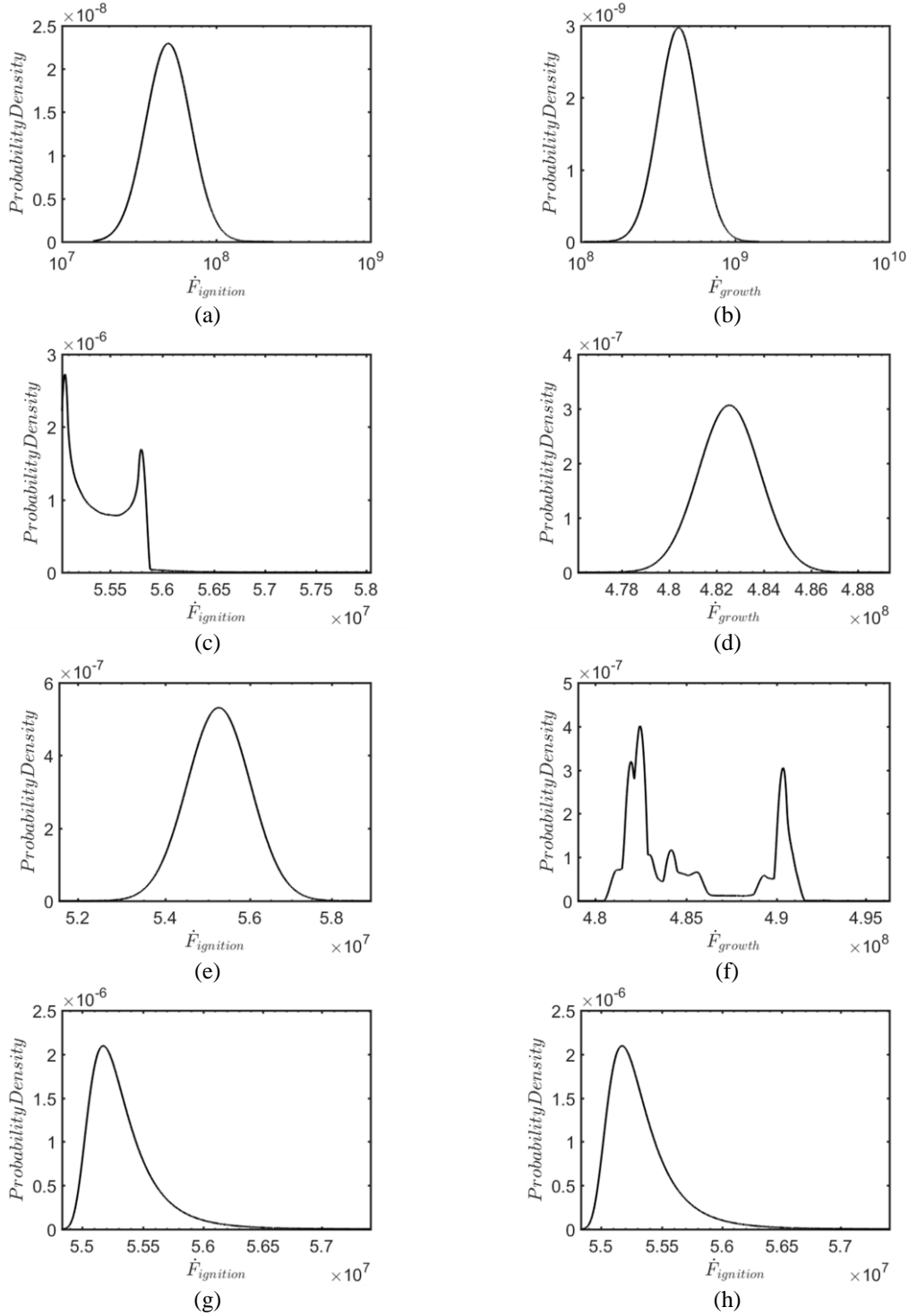
Figure 8 : Conditional pdfs for $\dot{F}_{ignition}$ ((a),(c), (e), (g)) and $\dot{F}_{growth}$((b),(d), (f), (h)) computed at $P_S = 22\ GPa$ for the collapse of a single isolated cylindrical void of diameter $D_{void} = 0.5\mu m$. Figures (a), (c), (e) and (g) show the pdfs for $\dot{F}_{ignition}\big(\tilde{C}_P|\mu_\alpha,\mu_Y,\mu_{BM}\big)$, $\dot{F}_{ignition}\big(\tilde{\alpha}|\mu_{C_P},\mu_Y,\mu_{BM}\big)$, $\dot{F}_{ignition}\big(\tilde{Y}|\mu_{C_P},\mu_\alpha,\mu_{BM}\big)$ and $\dot{F}_{ignition}\big(\widetilde{BM}|\mu_{C_P},\mu_\alpha,\mu_Y\big)$ respectively, while Figures (b),(d),(f) and (h) show the pdfs for $\dot{F}_{growth}\big(\tilde{C}_P|\mu_\alpha,\mu_Y,\mu_{BM}\big)$, $\dot{F}_{growth}\big(\tilde{\alpha}|\mu_{C_P},\mu_Y,\mu_{BM}\big)$, $\dot{F}_{growth}\big(\tilde{Y}|\mu_{C_P},\mu_\alpha,\mu_{BM}\big)$ and $\dot{F}_{growth}\big(\widetilde{BM}|\mu_{C_P},\mu_\alpha,\mu_Y\big)$ respectively.
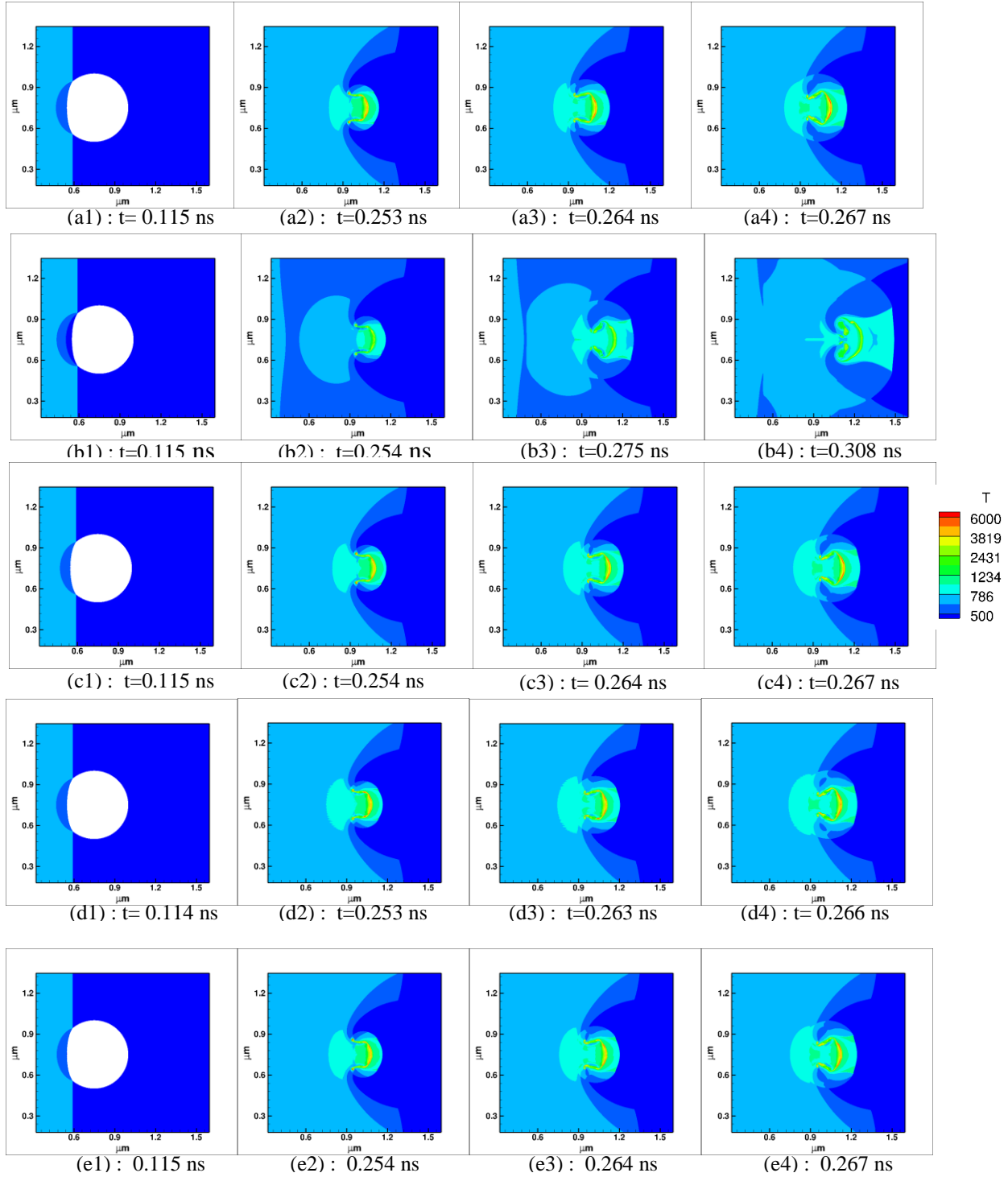
Figure 9 : Temperature contours in K at different stages of the collapse of a void of diameter $D_{void} = 0.5\mu m$ when impacted by a shock of $P_s = 22GPa$. The contours are shown for $[C_p, K_T, \sigma_Y, \alpha] = [1800\,J/KgK, 10.8545\,GPa, 0.249\,GPa, 20.05 \times 10^{-5}\,/K]$, $[2300J/KgK, 10.8545\,GPa, 0.249\,GPa, 20.05 \times 10^{-5}\,/K]$, $[1800JKgK, 16.4\,GPa, 0.249\,GPa, 20.05 \times 10^{-5}\,/K]$,$[\,1800J/KgK, 10.8545\,GPa, 0.37\,GPa, 20.05 \times 10^{-5}\,/K]$ and $[1800J/KgK, 10.8545\,GPa, 0.249\,GPa, 27 \times 10^{-5}\,/K]$ in (a) through (e). The instances 1 and 2 denote the start and end of the ignition phase, while the instances (3) and (4) denote the start and end of the growth phase in cases (a) through (e).
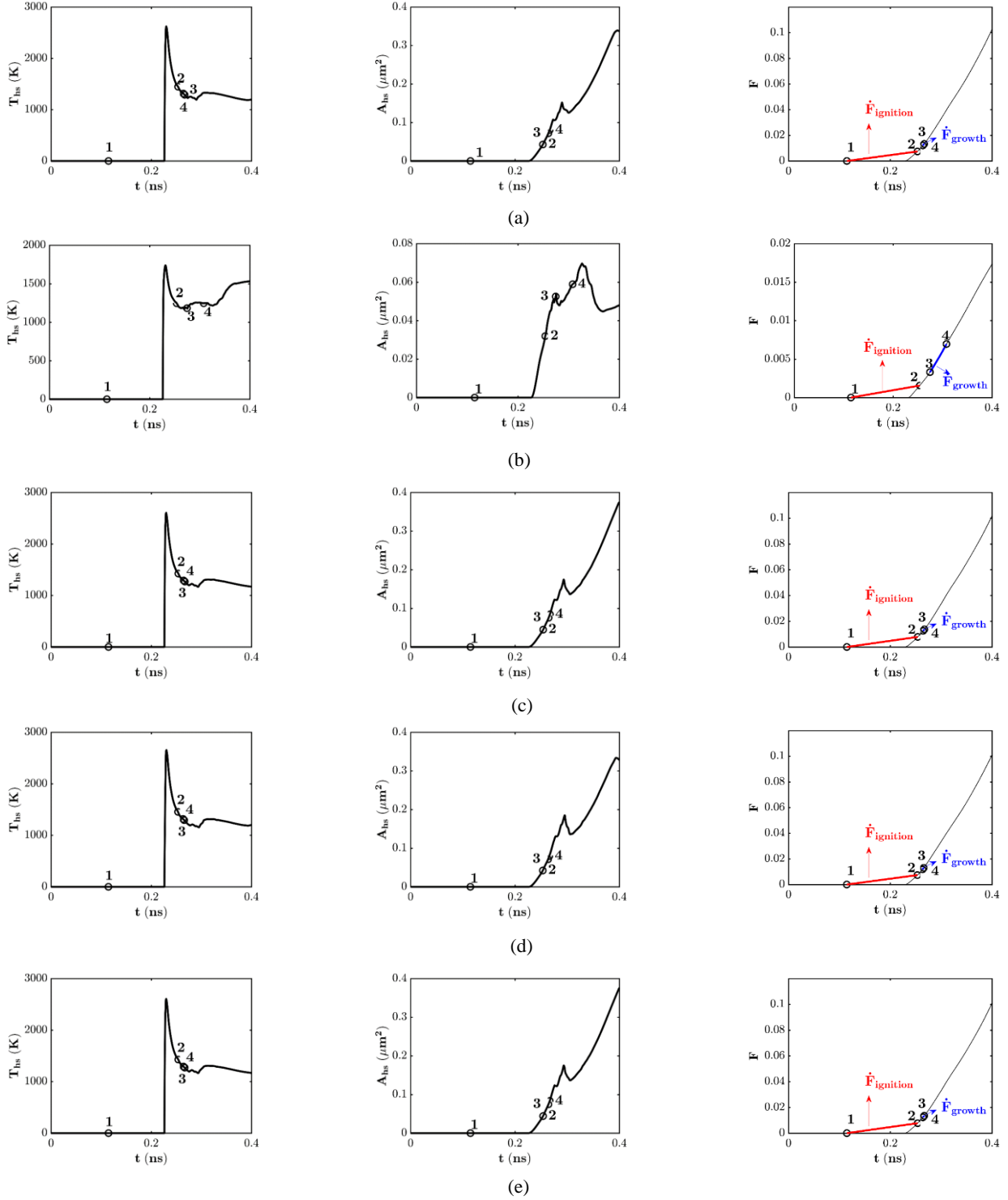
Figure 10: Evolution of the hot-spot temperature (T_{hs}) and area (A_{hs}), and the meso-scale product formation rate, F at different stages of the collapse of a void of diameter $D_{void} = 0.5\mu m$ for $P_s = 22 GPa$. The plots are for $[C_p, K_T, \sigma_Y, \alpha] = [1800\ J/KgK,\ 10.8545\ GPa,\ 0.249\ GPa,\ 20.05 \times 10^{-5}\ /K]$, $[2300J/KgK,\ 10.8545\ GPa,\ 0.249\ GPa,\ 20.05 \times 10^{-5}\ /K]$, $[1800JKgK,\ 16.4\ GPa,\ 0.249\ GPa,\ 20.05 \times 10^{-5}\ /K]$,$[\ 1800J/KgK,\ 10.8545\ GPa,\ 0.37\ GPa,\ 20.05 \times 10^{-5}\ /K]$ & $[1800J/KgK,\ 10.8545\ GPa,\ 0.249\ GPa,\ 27 \times 10^{-5}\ /K]$ in (a) through (e). Instances 1 and 2 denote the start and end of the ignition phase, while instances (3) and (4) denote the start and end of the growth phase in cases (a) through (e).
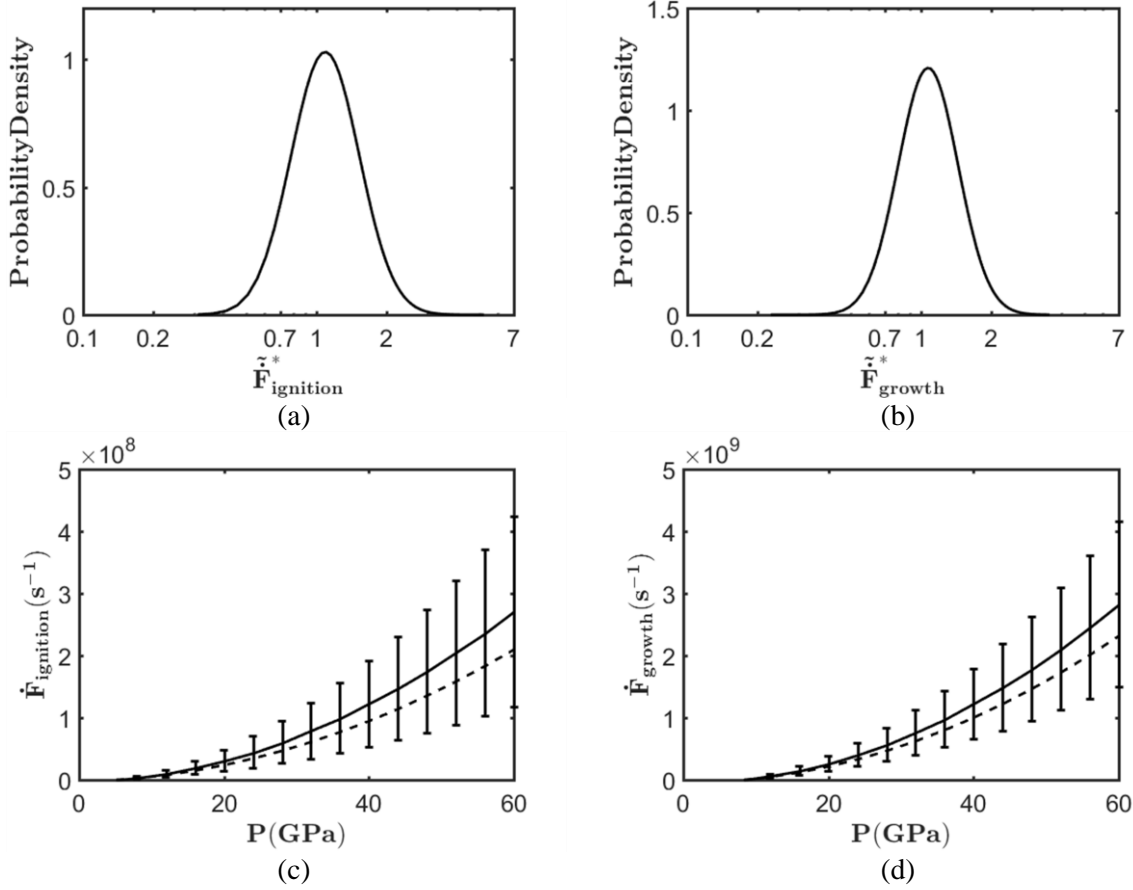
Figure 11. Probability density functions (a) $\tilde{F}^*_{ignition}$ and (b) $\tilde{F}^*_{growth}$ computed using Eqn. (9). Figure (c) shows the surrogates $\dot{F}_{ignition}(P_s; \mu_\pi)$ (in dotted lines) and $\tilde{F}_{ignition}(P_s)$ (in solid lines). Figure (d) shows the surrogates $\dot{F}_{growth}(P_s; \mu_\pi)$ (in dotted lines) and $\tilde{F}_{growth}(P_s)$ (in solid lines). The error bars in (c) and (d) represent the 90% confidence intervals with equal tail sets for $\tilde{F}_{ignition}(P_s)$ and $\tilde{F}_{growth}(P_s)$.
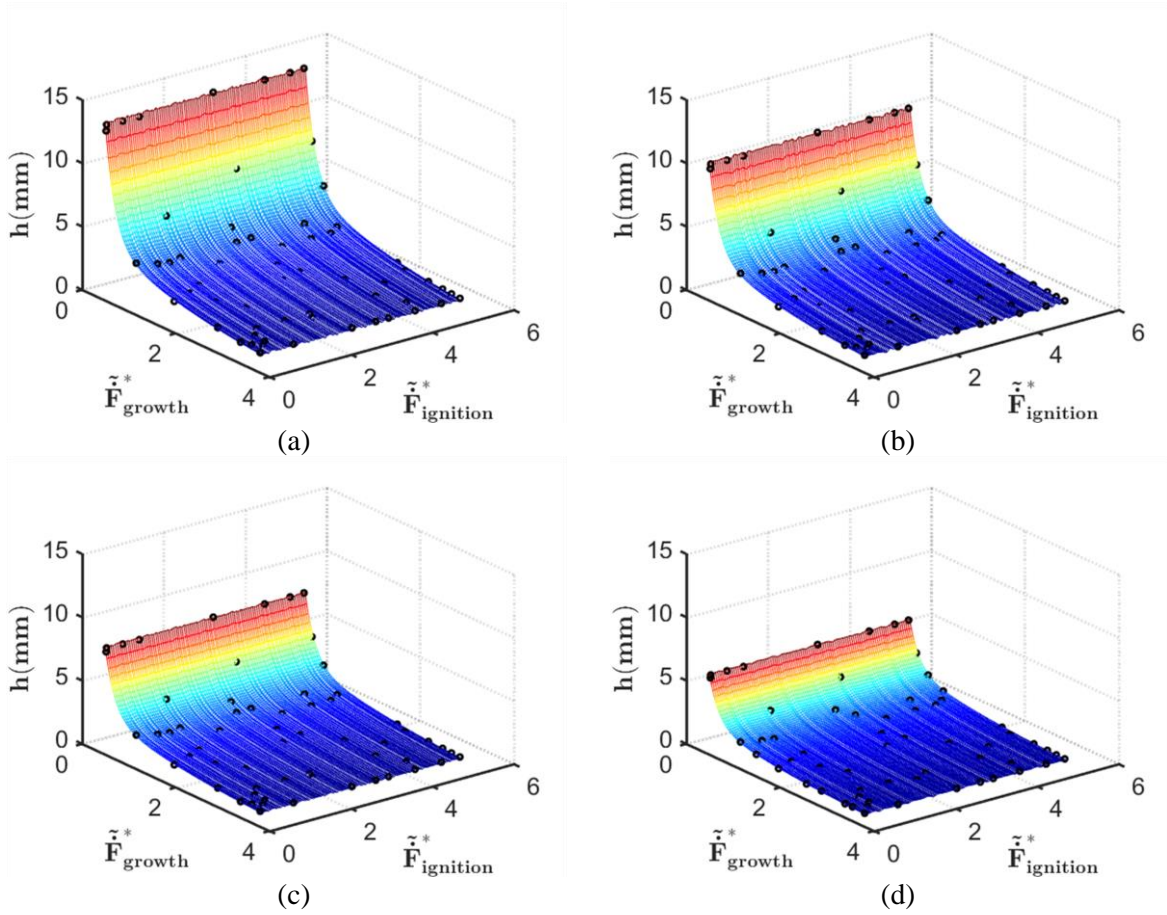
Figure 12 Surrogates for run-to-detonation distances h computed at $P_s =$ (a) $10 GPa$, (b) $12 GPa$, (c) $15 GPa$ and (d) $20 GPa$ as functions of $\tilde{\dot{F}}^*_{ignition}$ and $\tilde{\dot{F}}^*_{growth}$.
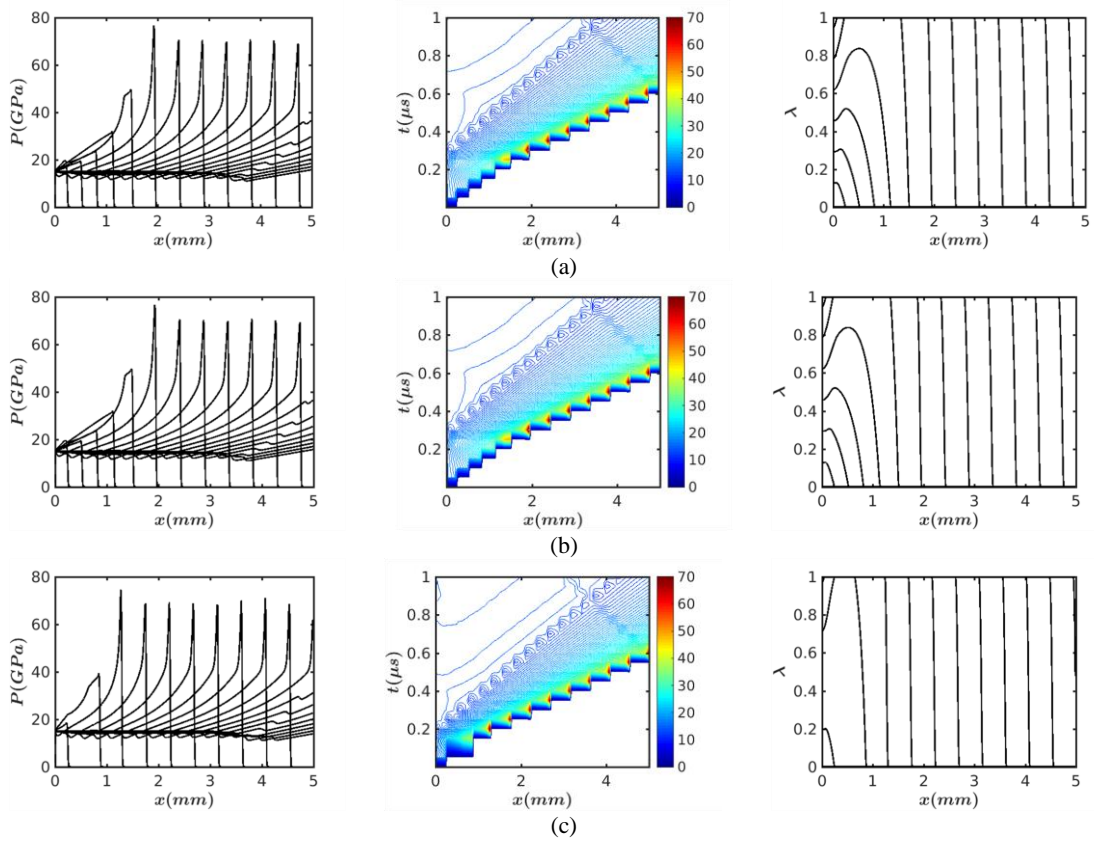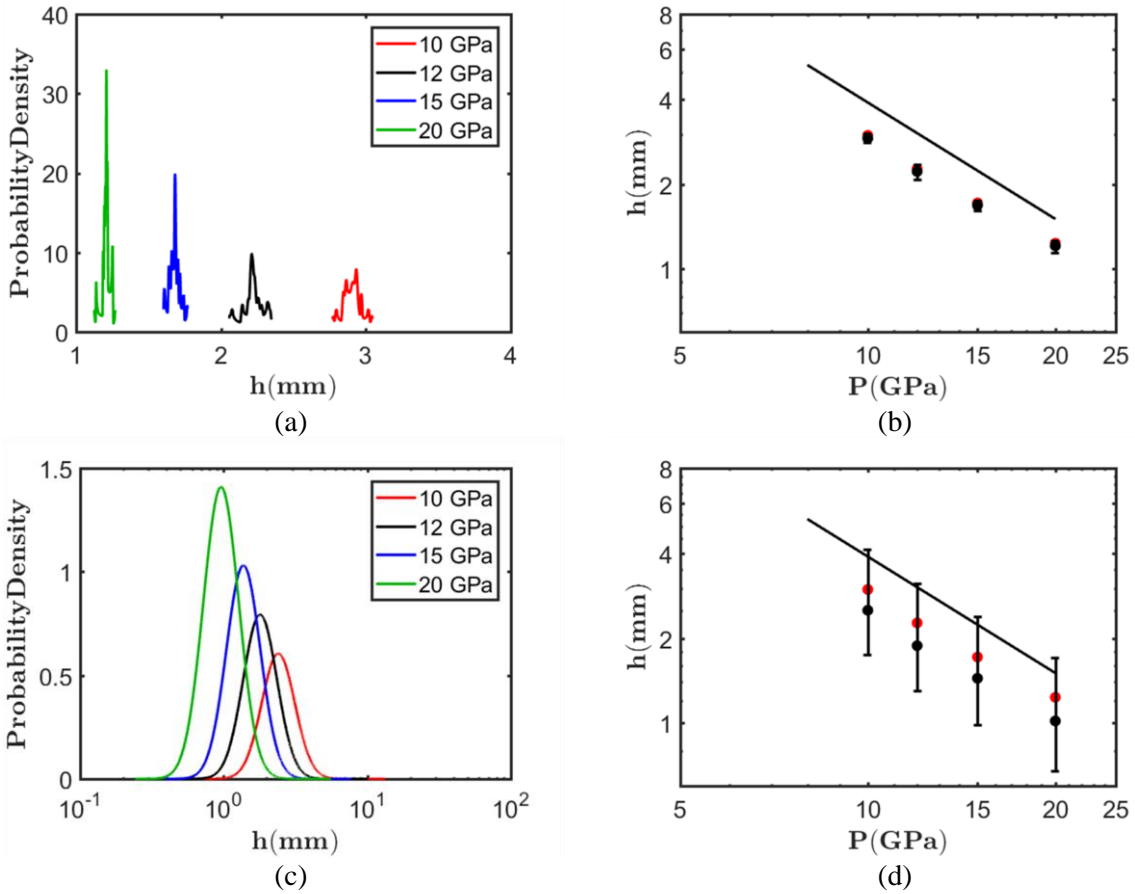
Figure 13 :

Figure 14. The conditional probability density functions (a) $\tilde{h}\left(\tilde{F}^*_{ignition}|\mu_{\tilde{F}^*_{growth}}\right)$ and (c) $\tilde{h}\left(\tilde{F}^*_{growth}|\mu_{\tilde{F}^*_{ignition}}\right)$ constructed at $P_s = 10, 12, 15$ & 20 GPa. The solid black dots in Figures (b)-(d) show the pop-plots obtained from the MES-IG model using the pdfs $\tilde{h}\left(\tilde{F}^*_{ignition}|\mu_{\tilde{F}^*_{growth}}\right)$ and $\tilde{h}\left(\tilde{F}^*_{growth}|\mu_{\tilde{F}^*_{ignition}}\right)$ respectively. The error bars denote the 90% confidence intervals with equal tail-sets. The red-dots show the pop-plots obtained from the deterministic MES-IG model, i.e. by performing RTD computations at $\tilde{F}^*_{ignition} = \mu_{\tilde{F}^*_{ignition}}$ and $\tilde{F}^*_{growth} = \mu_{\tilde{F}^*_{growth}}$. The solid line are the run-to-detonation distances observed in the experiments of , as reported by Massoni et al .
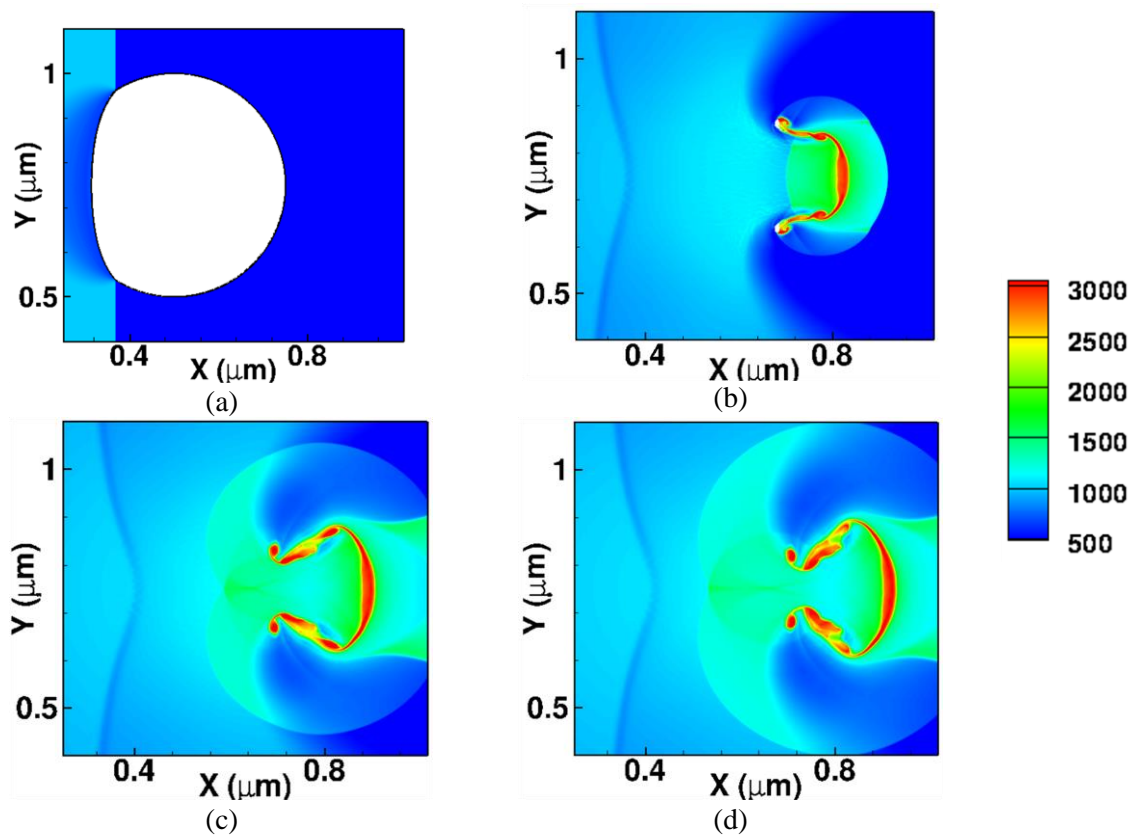
Figure 15: Temperature contours (in K) from a representative meso-scale computation of the collapse of a 0.5 μm void. The simulation performed by loading the solid HMX material with a pressure of 22.1 GPa. (a), (b), (c) and (d) are the contours at 0.06 ns, 0.18 ns, 2.05 ns and 2.15 ns respectively.
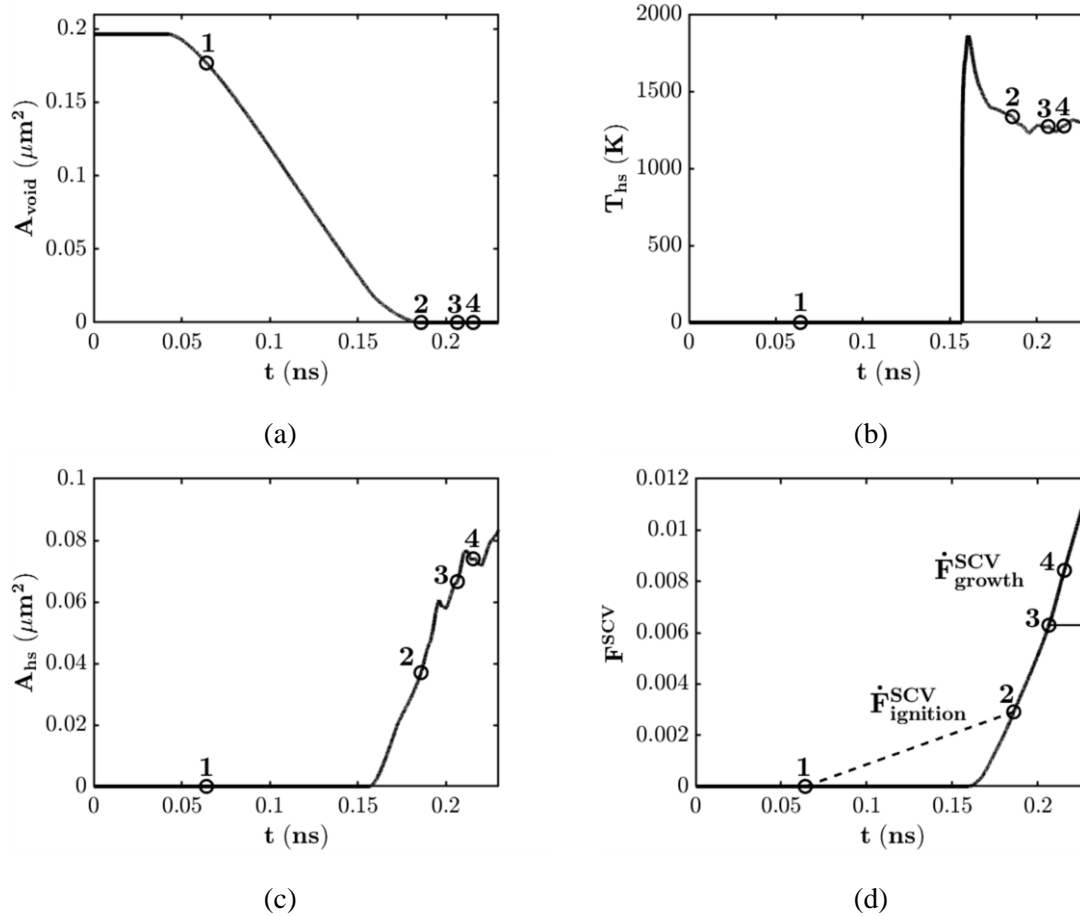
Figure 16. Illustration of the procedure for obtaining $\dot{F}^{scv}_{ignition}$ and $\dot{F}^{scv}_{growth}$ from the mesoscale numerical experiments. The illustration is shown for $D_{void} = 0.5$ μm, subjected to a shock pressure of $P_s = 22.1$ GPa. The figures show the variation of (a) void area, (b) hotspot average temperature, (c) hotspot area, and (d) the products mass fraction F with time. The numbers 1 through 4 in (a)-(d) indicate different instances of void and hot-spot formation/growth. In Figure (d), the time instances selected for computing the slopes to obtain $\dot{F}^{scv}_{ignition}$ and $\dot{F}^{scv}_{growth}$ are shown.